The $z=2.72$ galaxy cB58: a gravitational fold arc lensed by the cluster MS 1512 + 36

Stella Seitz,[1] R. P. Saglia,[2] Ralf Bender,[2] Ulrich Hopp,[2] Paola Belloni[2] and Bodo Ziegler[2]

[1]*Max-Planck-Institut für Astrophysik, PO Box 1523, D-85740 Garching, Germany*
[2]*Universitätssternwarte München, Scheinerstr. 1, D-81679 München, Germany*

ABSTRACT
Using *HST* WFPC2 *V*- and *R*-band data of the $z=0.37$ cluster MS 1512 + 36, we show that the $z=2.72$ 'protogalaxy' cB58 is not extraordinarily luminous intrinsically but lensed into a gravitational fold arc by the cluster. The arc has a surface-brightness-weighted axis ratio of 1:7, is marginally resolved in width and about 3 arcsec long. Its counterimage was identified and found to be very compact ($r_{1/2}=2.4$–4.0 h_{50}^{-1} kpc in a $q_0=0.05$ cosmology). In addition, we found three further multiple image systems, one with five and two with three images each. The positions of the multiple images can be explained by modelling the light deflection caused by the cluster and the cD galaxy with elliptical isothermal potentials. The major axis of the cluster potential approximately agrees with that of the cD light and that of the X-ray isophotes. As the multiple images are within ≈ 8 arcsec around the cD galaxy, a cluster core radius–cluster velocity dispersion degeneracy arises. Interpreting the observations conservatively, the cluster velocity dispersion and the core radius are limited to 540–670 km s^{-1} and 5–11 arcsec, respectively, and the brightness of the unlensed counterimage of cB58 is about 23.9 ± 0.3 (*R* band), corresponding to a magnification- and extinction-corrected rest frame *B*-band absolute magnitude of -24.75 ± 0.7 mag. The redshifts of the sources of the remaining three multiple image systems are predicted to be similar to that of cB58, while a strict upper limit of 4 is set as they are visible in *B*-band ground-based data. That part of the source of cB58 that is mapped into the arc is reconstructed and its magnification is found to be $\mu_{\mathrm{arc}} \gtrsim 50$. This large magnification explains at least some of the untypical spectroscopic properties of cB58, e.g. that the star formation rate seems to be high and uniform and to take place in a large area.

Key words: galaxies: clusters: individual: MS 1512 + 36 – galaxies: fundamental parameters – galaxies: individual: cB58 – dark matter – gravitational lensing.

1 INTRODUCTION

The $z=2.72$ galaxy cB58 – discovered by the (ground-based) CNOC survey of cluster redshifts (Carlberg et al. 1996a,b) – is one of the brightest ($m_V \approx 20.6$) high-redshift galaxies presently known. According to Yee et al. (1996, hereafter Y96) the galaxy is a well-resolved 3 arcsec $\times$ 2 arcsec disc-like galaxy, and thus the size of the galaxy is also surprisingly large for its redshift. Several strong absorption lines were identified in the rest-frame wavelength range of

$1000 \leq \lambda \leq 2000$ Å, which are characteristic for a young stellar population. Using multicolour photometry, Y96 and Ellingson et al. (1996) investigated its spectral energy distribution in a broader range, i.e. between $\lambda = 5000$ and $21\,000$ Å. From SED models of Bruzual & Charlot (1993) they inferred that a substantial fraction of the stellar component of the galaxy is younger than 10 Myr, and that the extinction-corrected and model-dependent star formation rate has to be of order 4700 M$_\odot$ yr^{-1}. Owing to the homogeneous appearance of the galaxy, the stars have to form

uniformly in the galaxy. Thus, they conclude that cB58 is a galaxy in its initial star-formation stage and call it a 'proto-galaxy'. A large magnification by gravitational lensing, which would decrease the 'true' magnitude, size and star-formation rate of the galaxy, was discarded as unlikely because of the 'resolved, regular and smooth nature of the object'.

Since the galaxy cB58 lies only 6 arcsec from the central galaxy of the cluster MS 1512 + 36 at $z = 0.373$, Williams & Lewis (1997, hereafter WL) investigated the possibility that cB58 is a 'normal' $z \approx 3$ star-forming galaxy magnified by the cluster. According to WL, a magnification of $\mu \approx 40$ is sufficient to decrease the observed non-extinction-corrected star-formation rate of $400\,M_\odot\,\mathrm{yr}^{-1}$ to that value found by Steidel et al. (1996a) for $z > 3$ galaxies and by Ebbels et al. (1996) for arcs in galaxy clusters. The mass distribution of the cluster was modelled as an isothermal sphere with a core. A velocity dispersion of $\sigma = 1000$ km s^{-1} and a core radius of 22.2 arcsec provides a (fine-tuned) model for the mass distribution, with a large magnification of $\mu \approx 40$ but a small shape distortion at the position of cB58, and avoids the prediction of multiple images, which were not observed from ground.

The velocity dispersion used in WL is in conflict with the measured value of (690 ± 100) km s^{-1} by Carlberg et al. (1996a), with a 90 per cent confidence interval of $602 \leq \sigma/$km s$^{-1} \leq 840$ (Carlberg, private communication). The core radius of $\approx 140\,h_{50}^{-1}$ kpc exceeds that of the most detailed modelled and more massive clusters, e.g. A370 (Mellier et al. 1990; Kneib et al. 1993) or A2218 (Kneib et al. 1994, 1996), by 50 per cent and a factor of 3.5, respectively.

In this paper we present two-colour WFPC2 *HST* observations. In contrast to the ground-based data used by Y96, one can infer from the high-resolution WFPC2 data that although the cluster is poor in terms of velocity dispersion and optical richness it is able to distort strongly and produce multiple images of high-redshift galaxies, and that cB58 is a gravitational fold arc. In Sections 2, 3 and 4 we describe the observations and the observed properties of the cluster, some of its galaxies and all multiple-image systems found. The positions of the multiple images are used for the lens modelling in Section 5, where limits on the magnification of the counterimage of cB58 are also derived. The magnification of the arc cB58 is estimated in Section 6. Section 7 provides a weak lensing analysis which serves as a consistency check for the estimated velocity dispersion. The results are summarized and discussed in Section 8.

2 OBSERVATIONS

The cluster MS 1512 + 36 was observed with *HST* as part of a programme to study the evolution of the Fundamental Plane of elliptical galaxies as a function of redshift and to constrain the geometry of the Universe (Bender et al. 1998). Using the WFPC2 and the filters F555 and F675, three orbits were cumulated for each filter for a total of 6.3 and 5.8 ks, respectively. The exposure time was split into nine dithered images per filter to increase the resolution of the final image. Three sets of three images were taken, with horizontal integer pixel shifts between the three images and vertical subpixel (1/2 and 1/4 of the WF pixel size) shifts between the sets, to allow an optimal cosmic-ray rejection.

Table 1. R and V magnitudes of objects as defined in the text (see Fig. 1).

Object	m_R	Δm_R	m_V	Δm_V	$V - R$
A1	20.29	+0.01, −0.03	20.64	+0.02, −0.02	0.41
A2	22.83	+0.04, −0.07	23.23	+0.05, −0.06	0.40
B1	25.77	+0.27, −0.31	26.08	+0.16, −0.37	0.31
B2	25.69	+0.29, −0.25	25.90	+0.24, −0.26	0.21
B3	28.42	+1.64, −1.30	27.58	+0.45, −0.71	−0.84
I	24.08	+0.19, −0.18	24.22	+0.18, −0.22	0.27
C1	24.60	+0.20, −0.23	24.66	+0.20, −0.22	0.06
C2	24.98	+0.21, −0.21	24.98	+0.19, −0.19	0.00
C3	24.95	+0.28, −0.25	25.58	+0.17, −0.33	0.63
W1	24.42	+0.28, −0.27	24.78	+0.34, −0.38	0.36
W2	25.82	+0.27, −0.26	25.61	+0.46, −0.49	0.79
W3	24.73	+0.30, −0.32	24.02	+0.44, −0.39	0.29
WC	26.89	+1.12, −0.55	27.04	+0.68, −0.60	0.15
U	23.66	+0.09, −0.13	24.16	+0.10, −0.12	0.50
V	22.96	+0.06, −0.09	23.30	+0.14, −0.10	0.34
DB	22.64	+0.03, −0.06	23.80	+0.04, −0.08	1.16
S	20.60	+0.03, −0.04	21.08	+0.04, −0.06	0.48

The pipeline reduction was checked to be adequate. The images with integer pixel shifts were combined using the cosmic-ray rejection IRAF[1] algorithm, rebinned to a pixel size of one quarter of a WF pixel, aligned, averaged and rebinned to a pixel size of half a WF pixel, i.e. 0.0498 arcsec. The zero-point photometric calibration was computed following Holtzman et al. (1995) and found to be in agreement with ground-based photometry of the cluster (Ziegler 1996). The subsequent reduction was performed using MIDAS. The isophote shape analysis of the central cD galaxy allowed us to determine a first estimate of the position of the major axis of the cluster potential, using the algorithm of Bender & Möllenhoff (1987), adapted to the *HST* resolution. A model for the light distribution of the cD galaxy was constructed from the isophote shape analysis and subtracted from the images.

The magnitudes and colours of the gravitationally lensed galaxies described below were derived from these frames, computing both aperture photometry with appropriate apertures and annuli for the estimation of the sky value and isophote magnitudes. Table 1 gives the magnitudes and colours inside the 24.78 mag arcsec^{-2} isophote in the V band and 24.71 mag arcsec^{-2} isophote in the R band, corresponding to the 3σ limit above the sky. The errors are computed from the isophote magnitudes above 2σ and 4σ above the sky and reproduce the observed variations in the aperture magnitudes caused by photon statistics when different galaxy or sky apertures are used.

The Lucy–Richardson deconvolution algorithm (Lucy 1974) as implemented in MIDAS was applied to enhance the resolution across the gravitational arc cB58. 20 iterations were performed using the PSF generated by the TINY TIM software.

With the exception of the cD galaxy, all galaxy shapes were estimated using the SEXTRACTOR software (Bertin & Arnouts 1996).

3 THE CLUSTER AND THE cD-GALAXY

Fig. 1 shows the core of the cluster MS 1512 + 36 using coadded *V* and *R* data. The cluster is dominated optically by its cD galaxy (centre of Fig. 1). The measured velocity dispersion of the cD galaxy equals 260 ± 20 km s^{-1}, and increases to $\sigma_{cD} = 286 \pm 20$ km s^{-1} after aperture correction (Ziegler & Bender 1997). The results of the isophote shape analysis of the cD galaxy are shown in Fig. 2.

Note that the position angle and eccentricity of the light from the halo of the cD are not constant but both increase in the outer parts of the cD. From Fig. 2 we derive an axis
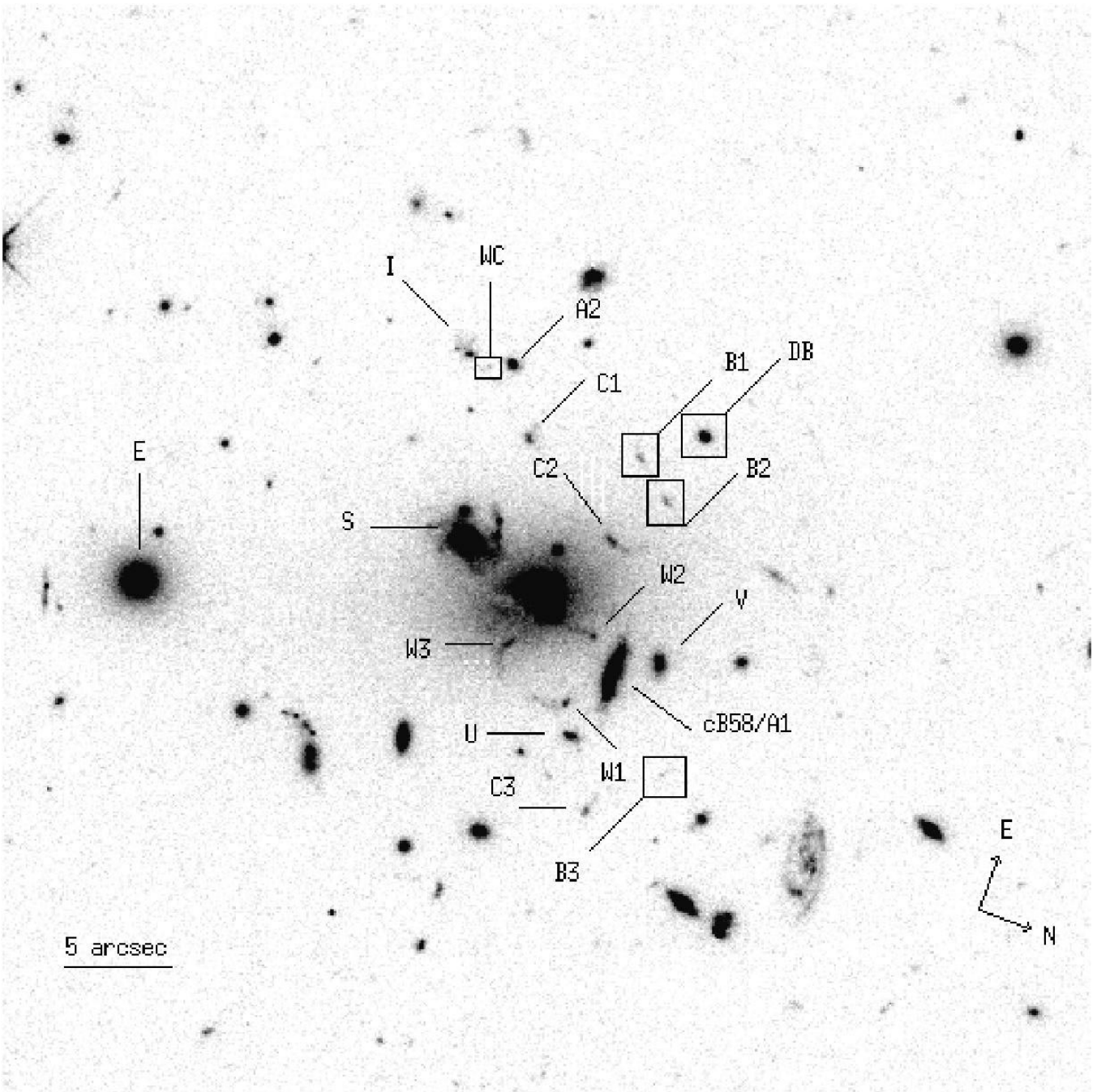

Figure 1. Image of the core of the cluster MS 1512 + 36 using coadded *V* and *R* data. Close to the cD galaxy in the centre is a face-on spiral S to its left. The galaxy cB58 is on the opposite side at 5 arcsec distance with an inclination angle of 71.6° relative to the *x*-axis. The compact bright object A2 at $(r, \phi) \approx (11$ arcsec, 97°) is the counterimage of the gravitational arc cB58. Left of the upper and lower end of cB58 are two shrimp-like objects (W1 and W2) with their heads pointing towards cB58. As argued in the text, they are also lensed, with a counterimage WC left of A2, and a fourth image at W3. Near the upper right diagonal of the field there is the galaxy pair B1 and B2. The counterimage candidate B3 with polar coordinates $(r, \phi) \approx (10$ arcsec, $-56°)$ relative to the cD is marginally visible in this figure. The three galaxies C1, C2 and C3 are most likely also multiply imaged galaxies.
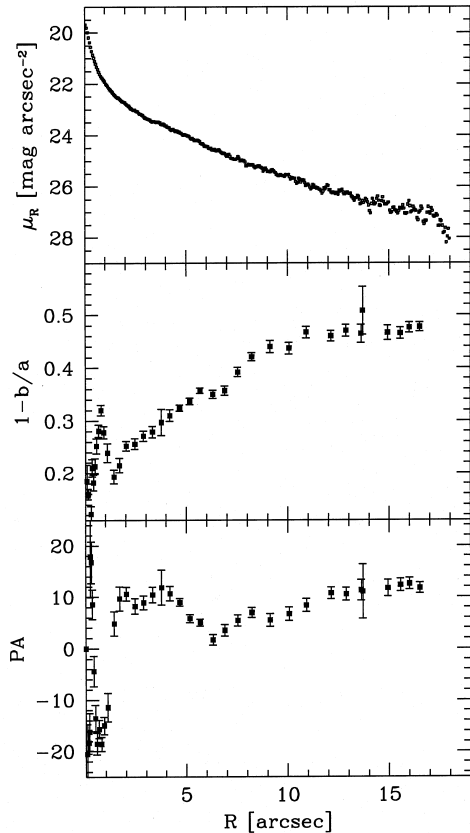
Figure 2. The isophote shape analysis of the cD galaxy. The top panel gives the circularly averaged surface brightness profile in the R band. The panel in the middle shows the ellipticity profile as a function of the circularized distance from the centre $R = \sqrt{ab}$. The panel at the bottom shows the position angle profile in degrees as a function of R.

ratio and major axis of the cD of $r = b/a = 0.7$ ($r = 0.6$) and $\phi = 10°$ ($\phi = 6°$) at a distance of 4 arcsec (7.5 arcsec) from its centre (angles are counted with respect to the x-axis of the WFPC3 chip). The major axis of the cD galaxy and that of the cluster potential – is inferred from X-ray photons – are roughly in agreement (compare with the X-ray map in Hamana et al. 1997). Similarly to the optical data, the X-ray map also shows a twist of the isophotes and an ellipticity change of the X-ray contours.

There is a face-on blue spiral galaxy with $m_V = 21.08$ and $m_{V-R} = 0.48$ at a distance of 4 arcsec from the cD galaxy. Absorption of the light from the halo of the cD near the spiral arms suggests that the spiral is in front of the cD. With only one colour it is quite difficult to estimate its photometric redshift. However, the irregular morphology of the galaxy, characterized by very bright and numerous H $_{II}$ star-forming regions, allows us to put some constraints on its spectral type and star-formation history. We modelled the stellar population of the galaxy using the GISSEL library for solar metallicity and Salpeter IMF (Bruzual & Charlot 1997), assuming an exponentially decreasing star-formation rate $\psi(t) = \tau^{-1} \exp(-t/\tau)$ with different time-scales ($7 < \tau < 10$ Gyr), and allowing for different return fractions for gas recycling (up to 40 per cent). We have assigned an age of 10 Gyr to the galaxy and considered the

evoluton of its spectral energy distribution for a set of cosmological parameters ($H_0 = 50, 70$ km s^{-1} Mpc^{-1}, $q_0 = 0.01, 0.1$). There are many uncertain parameters in these models, like the initial mass function (IMF), metallicity, dust etc. However, all galaxy models we considered indicate that the observed $V - R = 0.48$ can be matched either at $z \leq 0.35$ or at $z \approx 0.9$. The exponential scalelength of 1.1–1.3 arcsec clearly exludes the second hypothesis and thus the most probable redshift is $0.25 < z < 0.37 \equiv z_{cl}$. For this redshift range the R magnitude corresponds approximately to the rest-frame V magnitude and the luminosity of the galaxy is $0.8 L_* \leq L \leq 1.8 L_*$.

4 MULTIPLE IMAGES

Although the cluster is optically poor and dynamically weak, there are several strong and weak lensing signatures visible.

(i) As described by Y96, the galaxy cB58 (also denoted by A1 in the following) is at 5 arcsec distance from the centre of the cD; its V- and R-band magnitudes are $m_R = 20.29$ and $m_V = 20.64$, and its major axis position angle is $\phi_{A1} = 71.6°$. The galaxy is more elongated than visible from the ground (compare with fig. 2 in Y96). Its light distribution is slightly curved, with the centre of curvature not coinciding with the position of the cD, but pointing towards the outskirts of the cluster. Fig. 3 shows the Lucy–Richardson deconvolved light distribution of cB58 in the R band. The local background and rms noise are 1.2 and 0.4 count pixel^{-1}, respectively; hence the limiting contour of 5 count pixel^{-1} is 9.5σ above the background and the light distribution inside this contour is hardly affected by background noise. The mirror symmetry of the light distribution (the symmetry axis is sketched by the dashed line) indicates that cB58 is a merged image pair of a gravitationally lensed source. The gravitational arc is very elongated and only marginally resolved in width: perpendicular to the major axis the flux distribution of the galaxy is confined to 4–5 (dithered) pixels, and the flux increases steeply from the boundary towards the major axis. At the contour level of 5 count pixel^{-1}, the extent of the galaxy parallel to the major axis is about 50 pixel (2.5 arcsec). The SEXTRACTOR axis ratio obtained from the (eight) isophote-weighted second moments of the light distribution (within the same contour as the limiting isophote) is about 7. The unweighted ratio of the outermost isophote is about 1:10. This axis ratio also places a lower limit on the magnification of the arc, together with its unresolved width and assuming that the source of A1 is circular. The area enclosed by pixels with a surface brightness larger than 4 (5.5, 10) count pixel^{-1} is equal to 258 (210, 138) pixel.

(ii) There are several indications that the faint galaxies (B1, B2 in the following) at 8 arcsec distance from the cD galaxy belong to a multiple image system. The galaxies have similar morphologies and the same colours within the quoted errors (see Table 1). Thirdly, there is diffuse emission connecting the two galaxies, as expected when a faint part of the source lies on a caustic and thus is mapped into a gravitatinal arc, whereas the major part of the source is inside that caustic and is mapped into two images separated by the corresponding critical line. From the $V - R \approx 0.2$ colour of B1 and B2 and from the reasonable assumption of
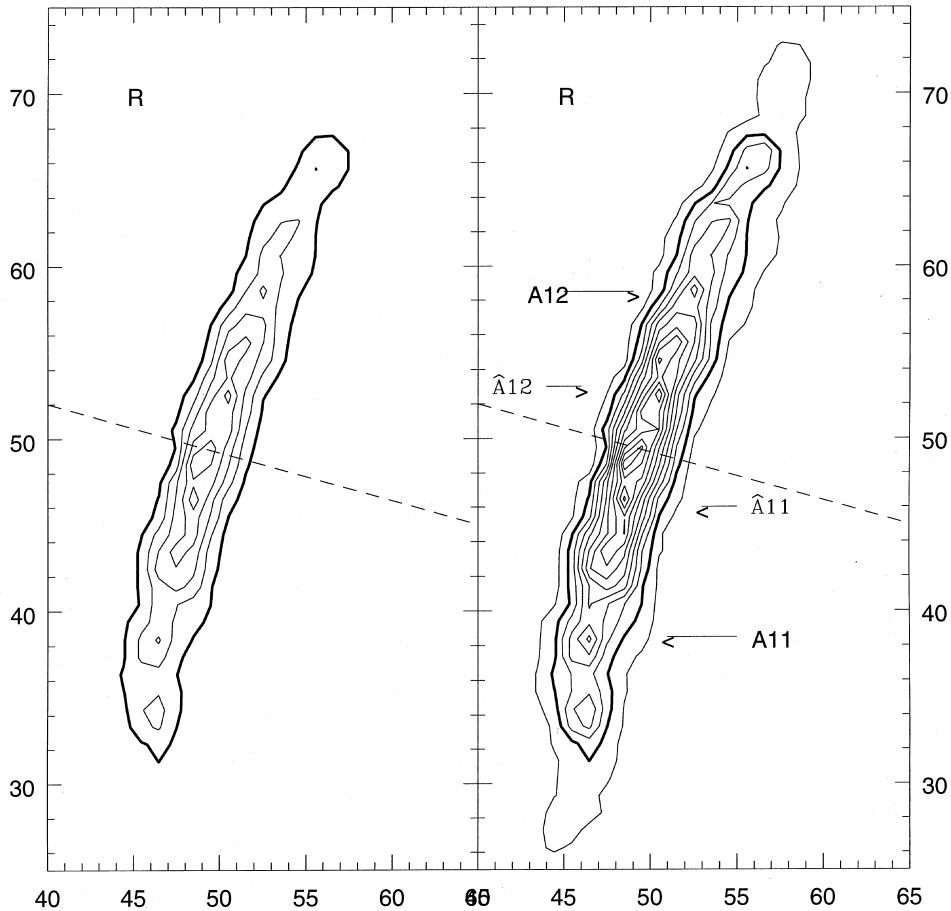
Figure 3. *R*-band counts for the galaxy cB58 obtained from the Lucy–Richardson deconvolved data. One unit in the horizontal and vertical direction equals one pixel of size ≈ 0.05 arcsec. Contours are spaced by 10 (left) and 5 (right) count pixel^{-1}; the thick line corresponds to a 10 count pixel^{-1}. The knots marked by A11, A12, Â11 and Â12 are used for the lens modelling later on.

their morphological (spiral) type, we estimate $z_B > 1.5$ as a lower limit for their redshifts with the GISSEL models as above. The upper limit is $z_B < 5$ because otherwise the rest-frame Lyman limit of the galaxies would drop out of the *V* band of the observers. The elliptical galaxy (DB) 3.2 arcsec apart from B1 coincides in colour (see Table 1) with that of spectroscopically confirmed cluster members (e.g. the elliptical E and the cD galaxy; for details about spectroscopy of cluster members see Carlberg et al. 1996a,b, Ziegler & Bender 1997). The $D_{n-\sigma}$ relation (Dressler et al. 1987) yields an estimate of 84 ± 15 km s^{-1} for its velocity dispersion. Hence, the galaxy DB is separated by about 22 Einstein radii from B1 and its light deflection on B1 and B2 could be neglected in the field or in regions where the cluster is weak. Near a critical line, however, the small shear induced by DB is sufficient to perturb it locally and thus to change the magnification and (slightly) the positions of B1 and B2. Therefore, the galaxy DB will be taken into account in the quantitative lens modelling below.

The parameters of a lens system can be determined most accurately if the corresponding counterimages of arcs or double images on the opposite side of the cluster are found, because this determines the enclosed mass most strongly (see, e.g., Mellier, Fort & Kneib 1993 for MS 2137 − 23, Kneib et al. 1994, 1996 for Abell 2218). Modelling the

cluster as an elliptical non-singular isothermal potential and the cD as an elliptical singular isothermal potential and fitting the positions of the arc A1 and the pair B1 and B2 (with unknown redshift), we can predict the positions of the counterimage of A1 (denoted by A2) and that of B1 and B2, denoted by B3. Comparing our model with the observations we identify a galaxy as the counterimage A2 and a candidate for the counterimage B3.

(iii) The galaxy A2 is the compact object at the upper boundary of Fig. 1 and, more expanded, the bright object at the right of Fig. 4. Its magnitudes are $m_R = 22.83$ and $m_V = 23.23$; it is the only object in that region where the counterimage is expected and the colour of which agrees with that of A1 (see Table 1). The galaxy to the left of A2 (denoted by I) is too blue to be the counterimage. The contours for the counts per pixel in the *R* and *V* bands can be seen in the lower left and lower right parts of Fig. 5. The high-surface-brightness core of A2 is unresolved. In the *R* band, the surface brightness of 4 (5.5, 10) count pixel^{-1} is only exceeded within 27 (16, 3) pixels. A comparison of the area enclosed by the same contours in A1 shows that the arc area is ≥ 46 (approx. 13, approx. 10) times that of the counterimage for contours of 10 (5.5, 4) counts per pixel. From the magnitudes of A1 and A2 we obtain a magnification ratio of A1 to A2 of $\mu_{A1/A2} \approx 11$. Hence we conclude that the
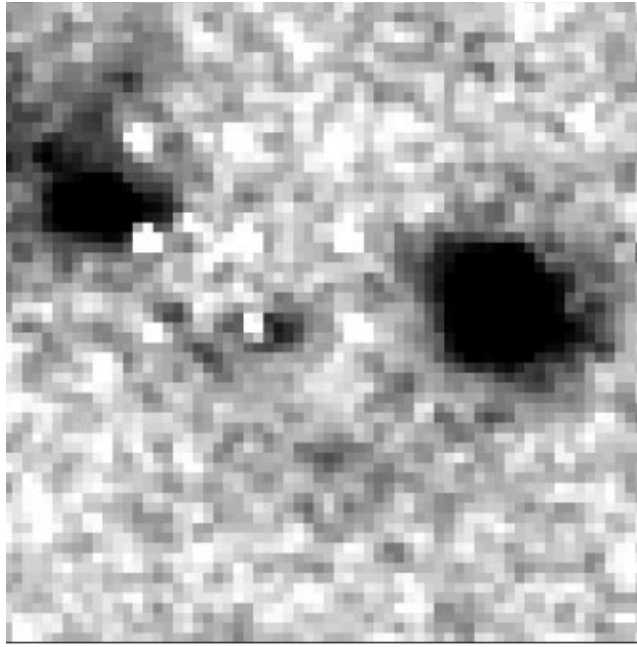
Figure 4. The right object in this part of the $V + R$ coadded image is the counterimage A2 of the gravitational arc cB58; the left object (1) is considerably bluer than A2. The grid of nine white pixels is caused by one bad pixel and reflects the nine different dither positions in the coadded $V + R$ exposures. The small object (WC) between A2 and I has a morphology similar to the 'shrimps' W1 and W2 visible in Figs 1 and 6. We consider this as the counterimage candidate of W1 and W2.
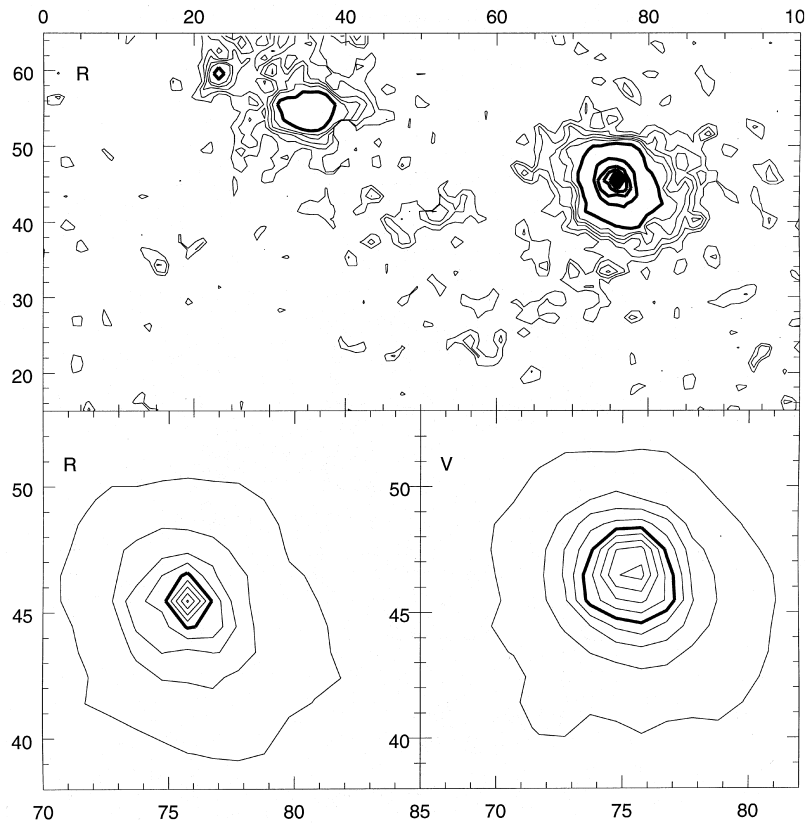

Figure 5. The upper part of this figure shows R-band contours of count pixel^{-1} within approximately the same region as seen in Fig. 4. The thin curves represent low signal-noise ratio contours with 1.35, 1.45, 1.55, 1.65 and 1.75 count pixel^{-1}; the object WC seen in Fig. 5 can barely be recognized. The thick contours start at 2 count pixle^{-1} and increase in steps of 2, thus flagging the high signal-to-noise ratio objects A2 and I. The surface brightness of A2 increases steeply towards its centre in the R band (lower left) and the V band (lower right). Here, the contours also start at 2 count pixel^{-1} and increase in steps of 2; the thick contour is that of 10 count pixel^{-1}.

high-surface-brightness core of the source of A1 and A2 lies on the caustic and is magnified most strongly, whereas the other remaining regions of the source are magnified only moderately, and parts of it are only singly imaged (into A2).

(iv) The candidate B3 for the counterimage of B1 and B2 can be seen in Fig. 1 as well. As its flux is not much above the noise level in *R*, the magnitude there can be measured only with a large error. This is less severe in the *V* band; the colour of B3 agrees within the large errors with that of B1 and B2. The galaxy in the rectangle in Fig. 1 is the only object above the 5σ detection limit of $V = 28.2$ the position and colour of which are compatible with being the counterimage B3. Although there is a galaxy near B3 as bright as DB (but bluer) for the case of B1 and B2, the additional light deflection caused by this galaxy will not be considered, because the cluster is non-critical at B3.

(v) To the left of the upper and lower end of cB58 (see Fig. 1) are two shrimp-like objects [the lower (upper) one is denoted by W1 (W2)] pointing with their 'head' towards cB58. These two images have different parity and they are on opposite sides of the critical line defined by the flux distribution of the arc (see Fig. 3). Hence, a lensing interpretation is most natural, and it suggests that the source redshift is similar to that of cB58. Simple lens models (using the positions of A1 and A2, B1 and B2 to determine the parameters of the cD and the cluster) indeed *predict* that W1 and W2 have a common source and a faint counterimage left of A2 if they are at the same redshift as A1. They also predict a fourth image (W3 in the following) to the left of W1 and W2, right at that point of blue emission that makes the W system appear as a circular structure. The position of the fifth image depends more on the details of the model: e.g. it can merge with the fourth image, causing the more extended 'head' of W3, or it could be a fainter image near the centre of the cluster. We can also identify the predicted counterimage of the W system with a noisy emission between the I and A2 galaxies in Fig. 4 (WC in the following). More details of the W system are given in Fig. 6

(using $V + R$ data). The left panel of this figure shows that the object WC is also 'shrimp-like' and has the same parity as W1. As the fluxes of W1, 3 and 3 in the *R* band are considerably affected by the red light of the cD galaxy, colour comparisons are difficult. As described before, a model for the light distribution of the cD galaxy was constructed from the isophote shape analysis and subtracted from the images. Especially near W3, the colour estimates may be affected by dust absorption caused by the nearby spiral. For W1, 2 and WC the colours agree within the error bars, which do not include systematic errors resulting from insufficient subtracted cD light. We conclude that the 'true' colour of the W system is likely to be that of W1 or WC, whereas W2 and W3 may be affected by inaccurate subtraction of the cD light.

(vi) The three galaxies C1 to C3 in Fig. 1 are most likely multiply lensed as well. C1 and C2 are on the opposite sides of the critical line for a $z \approx 2-3$ galaxy, as can be seen from an extrapolation of the critical line passing through B1 and B2 to the left. All of the three galaxies have a 'head' and a 'tail' inclined to the major axis of the head (see Fig. 7). C2 has opposite parity to C1 and C3. The colours of C1 and C3 do not support the lensing hypothesis (Table 1) because they only marginally agree within their 1σ errors. The ground-based data in the *B* band (Gioia & Luppino 1994) provided by G. Luppino neither contradict nor confirm the lensing hypothesis further; although C1, C2 and C3 are all visible in the data, the exposure is not deep enough to improve the accuracy on the colour determination. As the C galaxies as well as B1 and B2 are visible in the *B* band, we can estimate the upper limit of their redshifts to about $z_{max} = 4$.

Despite the slight inconsistency of the colour of C1 and C3, we consider C1, C2 and C3 as a multiple image system: for every lens model that reasonably fits the A, B and W system we *robustly predict* that C1 to C3 have a common source if their redshift is marginally larger than that of cB58. Additionally, the directions of the tails relative to the major
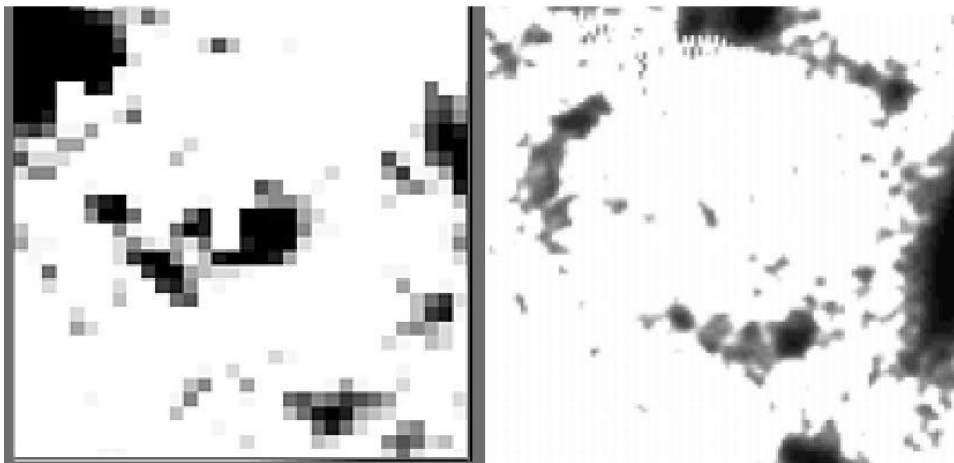

Figure 6. In the left panel one can see the counterimage candidate WC; although the signal-to-noise ratio for this object is low (even in the coadded $V + R$ data), one can identify the same shrimp morphology ('head' to the right and curved 'tail' to the left) as is seen in the objects W1 (lowest object), W2 (right object) and W3 (left object) in the right panel, where a model for the emission of the cD galaxy was subtracted.
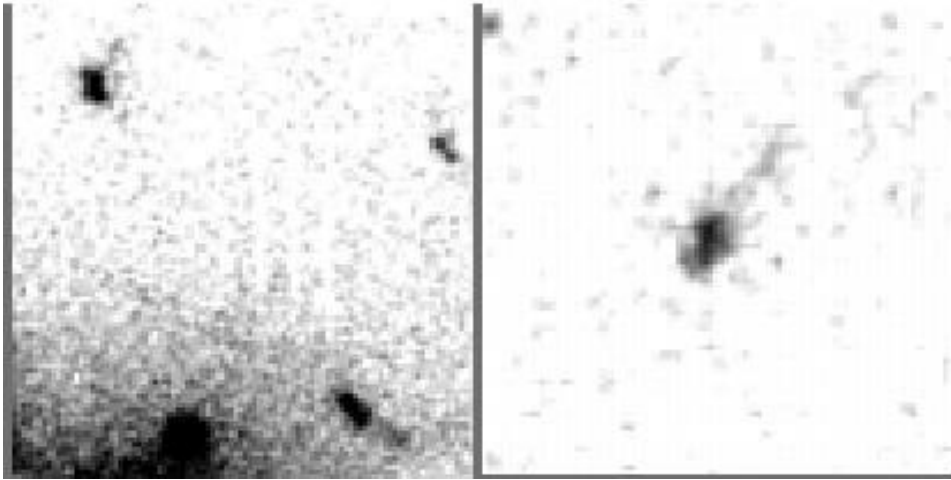
Figure 7. In the upper left and lower right corner of the left part of this figure C1 and C2 are visible. The suggested counterimage C3 (right part of the figure) coincides in morphology with C1 and C2: all objects consist of a 'head' and a 'tail' inclined to the major axis of the head. The parity of C1 and C2 is reversed. The relative orientation of the tail is predicted by lens models.

axis of the heads are also predicted as they are observed. It may happen accidentally that three sources are along the line of sight to three possible multiple image positions, but we consider it unlikely, because not only their relative morphology but also their relative orientation agrees with that predicted by gravitational lensing.

5   MODELLING THE LENS SYSTEM

The lens models investigated below are defined as superpositions of elliptical isothermal deflection potentials (see the Appendix) and they are described by the following parameters.

(i) The orientation ϕ_{cl}, ellipticity ϵ_{cl}, velocity dispersion σ_{cl} and core radius ζ_{cl} of the *cluster* will be treated as free parameters. The cluster centre is assumed to coincide with that of the cD galaxy.

(ii) The ellipticity and orientation of the *cD galaxy* are either treated as free parameters, assumed to be equal to that of the cluster or inferred from the light. In the second case the assumption is motivated by earlier investigations (e.g. Mellier et al. 1993), finding that the major axis of clusters dominated by a single mass concentration is aligned with that of the central galaxy. In the third case we assume that the major axis defined by the surface-brightness distribution of the extended emission of the cD coincides with that of the projected mass distribution. Using equation (A13) we obtain $\epsilon_{cD} = 0.06$ and $\phi_{cD} = 5\text{--}10°$. The core radius is assumed to be zero, whereas the velocity dispersion σ_{cD} of the cD galaxy is a free parameter.

(iii) Additional *galaxies* are treated as spherical singular systems ($\epsilon = 0$, $\zeta = 0$) with their velocity dispersion as free parameters.

5.1   The lens models

Let $\boldsymbol{p} = (p_1, \ldots, p_f)$ denote the free parameters of the lens model, K the number of multiply lensed sources, $I(k)$, where $k = 1, \ldots, K$, the number of images for each of the k sources;

further, let θ_{i_k} denote the position of the ith image $[1 \le i_k \le I(k)]$ of the kth source. For each image position the deflection angle $\boldsymbol{\alpha}(\theta_{i_k}; \boldsymbol{p})$ is calculated and a source position $\boldsymbol{\beta}_{i_k}(\boldsymbol{p}) := \boldsymbol{\beta}(\theta_{i_k}; \boldsymbol{p}) = \theta_{i_k} - \boldsymbol{\alpha}(\theta_{i_k}; \boldsymbol{p})$ is predicted. The best-fitting model is obtained by minimizing

$$E := \sum_{k=1}^{K} W(k) \sum_{i_k, i'_k = 1}^{I(k)} w(i_k)\, w(i'_k)\, |\boldsymbol{\beta}_{i_k} - \boldsymbol{\beta}_{i'_k}|^2 + f(P) \tag{1}$$

with respect to the free parameters of the model using the POWELL routine described by Press et al. (1992). $W(k)$ and $w(i_k)$ are weights equal to one or zero, and thus they determine which of the multiply imaged sources are considered [$W(k)$], and which of their images [$w(i_k)$] are taken into account for the model fitting. The additive function $f(P)$ is used to take into account parities P of images. (The photometry is too inaccurate to include flux ratios.)

The fold arc contains much more information than the position of its centre of light: the critical line passes through it and each pixel must have a corresponding pixel with the same surface brightness on the opposite side of the critical line. These pixel pairs will have a common source in the ideal case. The information contained in the light distribution of the arc will be used in more detail later on; if we only fit the position of the arc we simply choose two of these corresponding points (A11 and A12) on opposite sides of the critical line, require that they and A2 have a common source (A1) and that the parity of A11 and A12 is reversed. We use the positions of the knots (which have the same surface brightness) marked in Fig. 3 as A11 and A12. The use of the A11 and A12 positions together with the parity constraint requires the critical line to pass between A11 and A12, e.g. it rejects models where A11 and A12 belong to the same large segment of a giant tangential arc. The parity constraint is easily implemented by adding a term to equation (1) proportional to the product of the determinant of the Jacobian if this product is positive.

Thus, generally four kinds of observables can be used for the model fit: positions (A11, A12, A2, B1, B2, B3, W1, W2, WC, W3, C1, C2, C3), flux ratios, the parity of the lens map

Table 2. Best-fitting values ($+$) and assumed fixed values ($-$) for the cluster, the galaxies and the redshift of the objects. Velocity dispersions σ_{cl}, σ_{cD} σ_E are given in km s^{-1}. Major axis position angles Φ_{cl} and Φ_{cD} are given in degrees. The core radii ζ_{cl} are quoted in acrsec, where 0.0498 arcsec corresponds to one pixel. See Fig. 8 to convert the lensing strengths d_B, d_W, d_C into redshifts.

Model	σ_{cl}	ϵ_{cl}	ϕ_{cl}	ζ_{cl}	σ_{cD}	σ_{DB}	σ_S	σ_V	d_B	d_W	d_C	ϵ_{cD}	ϕ_{cD}	σ_E
start	710	0.0	8	5.0	286	84	0	0	1	1	1	0.06	10	176.0
MIa$^{(1a)}$	$+$ 569.1	$+$ 0.16	$+$ 11.3	$+$ 6.1	$+$ 246.3	$-$ 84	$-$ 0	$-$ 0	$-$ 1.	$+$ 1.002	$+$ 1.048	$+$ 0.08	$+$ 12.1	$-$ 176.0
MIb$^{(1b)}$	630.8	0.11	6.5	9.0	251.4	84	0	0	1.	0.9998	1.026	0.20	26.7	176.0
MIIa$^{(2)}$	$+$ 564.0	$+$ 0.20	$+$ 12.1	$+$ 7.0	$+$ 246.0	$+$ 0	$-$ 0	$-$ 0	$+$ 1.025	$+$ 1.0	$-$ 1.03	$+$ 0.00	$+$ 12.1	$-$ 176.0
MIIIa$^{(3)}$	$+$ 593.4	$+$ 0.18	$+$ 9.7	$+$ 7.9	$+$ 249.1	$+$ 72	$-$ 0	$-$ 0	$+$ 1.020	$+$ 1.0004	$+$ 1.037	$+$ 0.00	$+$ –	$-$ 176.0
MIVa$^{(4)}$	$+$ 585.0	$+$ 0.19	$+$ 12.2	$+$ 7.6	$+$ 247.0	$-$ 84	$-$ 0	$-$ 0	$-$ 1.020	$+$ 1.005	$-$ 1.035	$+$ 0.00	$+$ 18.5	$-$ 176.0
MVa$^{(5)}$	$+$ 571.7	$+$ 0.17	$+$ 11.8	$+$ 7.2	$+$ 268.4	$-$ 70	$-$ 0	$-$ 0	$+$ 1.024	$+$ 1.001	$+$ 1.042	$-$ 0.06	$-$ 10.0	$-$ 176.0
MVb$^{(5)}$	583.2	0.15	12.4	6.8	246.0	70	0	0	1.024	1.002	1.042	0.11	10.0	176.0
MVc$^{(5)}$	615.4	0.14	11.7	8.3	246.0	70	0	0	1.023	1.004	1.035	0.06	ϕ_{cl}	176.0
MVIa$^{(6)}$	$+$ 582.0	$+$ 0.16	$+$ 14.3	$+$ 8.0	$+$ 246.2	$+$ 7	$+$ 111	$+$ 104	$+$ 1.016	$+$ 1.007	$+$ 1.035	$+$ 0.13	$+$ 12.2	$-$ 176.0

(1a) Positions of A11/A12/A2, W1/W2/W3/WC, C1/C2/C3 fitted.
(1b) Positions of Â11/Â12/A2, W1/W2/W3/WC, C1/C2/C3 fitted.
(2) Positions of A11/A12/A2, W1/W2/W3/WC, B1/B2/B3 fitted.
(3) As (1a), with triple weight for C1/C2/C3.
(4) Positions of A11/A12/A2, W1/W2/W3/WC fitted.
(5) Positions of A11/A12/A2, W1/W2/W3/WC, B1/B2/B3, C1/C2/C3 fitted.
(6) Positions of A11/A2, W1/W2/W3/WC, B1/B2/B3, C1/C2/C3 fitted as well as the shape of the arc cB58.

Table 3. The quality of the best-fitting models. The quantities Δ_W^2, Δ_A^2, Δ_C^2, Δ_B^2 give the square position residuals (in pixels) as defined in equation (6); μ_2^A are the predictions for the magnification of A2 (counterimage of cB58); δ_{21}^C, δ_{31}^C, δ_{C1}^W, δ_{32}^B are the predicted magnitude differences for C2/C1, C3/C1, WC/W1 and B3/B2. The first line contains the observed magnitude differences in the V band. The uncertainties for thes magnitude differences can be obtained using Table 1.

Model	Δ_W^2	Δ_A^2	Δ_C^2	Δ_B^2	μ_2^A	δ_{21}^C	δ_{31}^C	δ_{C1}^W	δ_{32}^B
Observed	–	–	–	–	–	0.33	0.92	2.26	1.68
MIa	179.2	0.5	144.4	–	2.15	0.20	0.67	1.63	1.05
MIb	20.6	4.0	79.51	396.8	2.89	0.34	0.77	1.79	0.80
MIIa	22.7	6.0	40.8	20.8	2.18	0.21	0.70	1.79	1.27
MIIIa	226.4	54.0	11.8	1.2	2.37	0.19	0.73	1.68	1.42
MIVa	41.3	1.0	118.5	352.7	2.28	0.17	0.69	1.72	1.20
MVa	74.7	5.0	62.0	190.1	2.29	0.23	0.67	1.64	1.17
MVb	46.2	10.6	101.3	269.3	2.32	0.16	0.68	1.66	1.11
MVc	85.3	0.0	54.0	278.1	2.77	0.20	0.79	1.92	1.19
MVIa	43.6	1.4	116.4	246.0	2.39	0.12	0.71	1.63	1.28

at A11/A12 and B1/B2 and the flux distribution of the arc. In Table 2 one can read off all parameters used for the lens modelling, and whether they are varied ($+$) or kept constant ($-$). In the first case the number below the plus equals the best-fitting value, in the second case it equals the assumed fixed value. As discussed already, the lens model is described by the cluster (σ_{cl}, ϵ_{cl}, ϕ_{cl} and θ_{cl}), the cD galaxy (σ_{cD}, ϵ_{cD}, ϕ_{cD}), the possibly perturbing galaxies DB, V and S next to B1/B2, A2 and left of W3 (σ_{DB}, σ_V, σ_S), and the unknown lensing strengths

$$d_B = \frac{D_{ds}(B)}{D_s(B)} \left[\frac{D_{ds}(cB58)}{D_s(cB58)} \right]^{-1}, \tag{2}$$

$$d_W = \frac{D_{ds}(W)}{D_s(W)} \left[\frac{D_{ds}(cB58)}{D_s(cB58)} \right]^{-1}, \tag{3}$$

$$d_C = \frac{D_{ds}(C)}{D_s(C)} \left[\frac{D_{ds}(cB58)}{D_s(cB58)} \right]^{-1}, \tag{4}$$

of the lens for B, W and C relative to cB58. Here $D_{ds}(X)$ and $D_s(X)$ are the angular diameter distances from the cluster to a source X and from the observer to the source. The starting values used in the minimization are given in the first line of Table 3. They are motivated by prior knowledge in the case of σ_{cl}, σ_{cD} and σ_{DB}: i.e. by the best-fitting value for the velocity dispersion of Carlberg et al. (1996a,b), the measurement of the velocity dispersion of the cD by Ziegler & Bender (1997) and the estimate of σ_{DB} using the $D_{n-\sigma}$ relation, which gives 84 ± 15 km s^{-1}. If nothing else is stated we restrict the allowed range for the velocity dispersion of the cD in the minimization of equation (1) to 246 km s$^{-1} \leq \sigma_{cD}$ 306 km s^{-1} which is the 1σ interval for the observed uncorrected and aperture-corrected velocity dis-
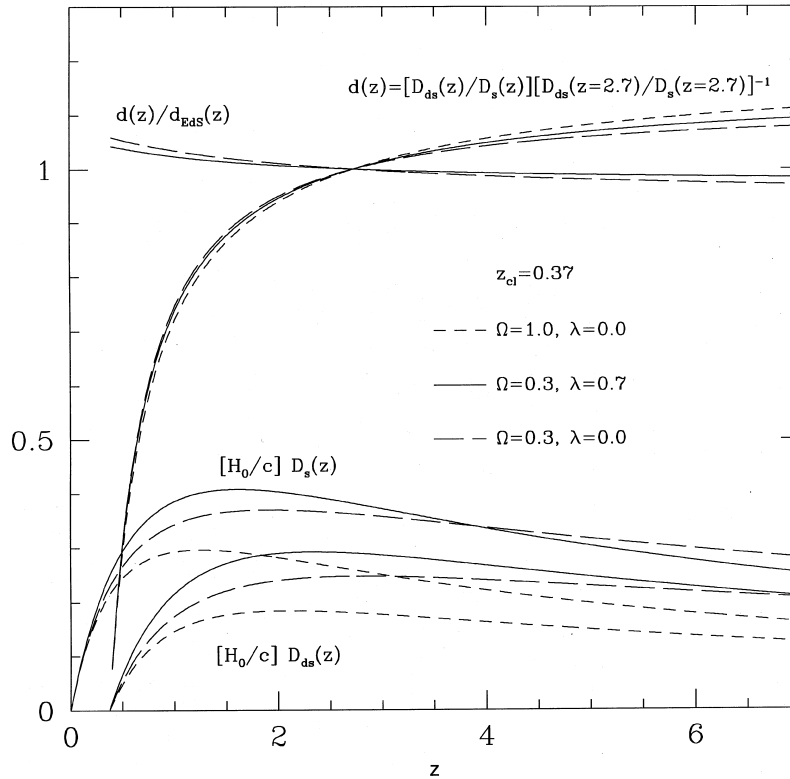
Figure 8. For three different cosmological models we have plotted the angular diameter distances from the observer (O) and the angular diameter distances from the cluster (C) to redshift z in units of the Hubble length (c/H_0): Einstein–de Sitter model (short-dashed), a low-Ω universe with $\lambda = 0$ (long-dashed) and with $\lambda = 1 - \Omega$. The redshift of the cluster is $z_{\gamma\mu} = 0.37$. The remaining three curves, which start at redshift $z = 0.37$ and are equal to zero there, show the lensing strength D_{ds}/D_s of a galaxy at redshift z in units of the lensing strength of the galaxy cB58 at $z = 2.7$, for the same three cosmological models. This ratio is called relative lensing strength *df* further on. The two flat curves show the relative lensing strength for the two low-Ω cases in units of the relative lensing strength for an Einstein–de Sitter universe.

persion of the cD. The ellipticity of the cluster and the cD is limited by $\epsilon_{cl} \leq 0.25$ and $\epsilon_{cD} \leq 0.2$. The role of the V galaxy will be discussed later; a velocity dispersion of $\sigma_V \leq 180$ km s^{-1} will be a safe upper limit irrespective of its redshift. The limiting values for d_B, d_W and d_C, $0.1 \leq d_X \leq 1.1$, only imply that the galaxies of the B, W and C system are behind the cluster and below a redshift of 5. To illustrate that, we have plotted the lensing strength for a galaxy at redshift z in units of the lensing strength for cB58 for three different cosmological models in Fig. 8 (for details concerning filled-beam angular diameter distances see Fukugita et al. 1992 and Asada 1996). In terms of lensing strength, a galaxy at $z = 2.7$ is almost at 'infinity' for a cluster at redshift $z = 0.37$; the lens is stronger only by 8 per cent for a galaxy at a redshift of 5 nearly independent of the cosmological model assumed.

Minimizing E in equation (1) implies that the distances between the source positions – estimated for all the members of a multiply lensed system – are minimized in the source plane. (In the ideal case the source separation is zero, because the galaxies are assumed to have a common source.) To estimate the quality of the best-fitting model $\hat{p}$ we define the 'mean' source for each image system as a disc with a radius of half a pixel, centred on

$$\hat{\beta}_k := \frac{1}{\sum_{i_k}^{I(k)} w(i_k)} \sum_{i_k=1}^{I(k)} \beta_{i_k}(\hat{p}) \, w(i_k). \tag{5}$$

With ray tracing we approximately invert the lens equation and solve for the extended images corresponding to the mean source. Let $\Delta(i_k)$ be the minimum distance of θ_{i_k} from the inverted extended images; we then define

$$\Delta_k^2 = \sum_{i_k=1}^{I(k)} |\Delta(i_k)|^2 \, w(i_k) \tag{6}$$

as the quadratic error of the fit. This error (divided by the number of images used for the fit) has to be compared with the error of image localization or the extent of the images at θ_{i_k}. Actually, Δ_k^2 should be minimized with respect to p to obtain the best-fitting model. Instead of this time-consuming process we minimize E (equation 1) and assume that the parameters that minimize E are not too different from those that minimize Δ_k^2. The fit quality of a model is quantified in Table 3. The first four columns contain the quadratic error of the fit in the lens plane, which was defined in equation (6). If a multiple *image system* (A, B, W or C) is used for the fit, then the weights in equation (5) are equal to that used in the minimization; this means that if one of the multiple images of the system is not used for the fit then it is also not used to estimate the fit quality. If an image system is not used for the fit, then Δ^2 measures the quality of the prediction that the observed images have a common source; in this case (if nothing else is stated) all its multiple image positions enter equation (6).
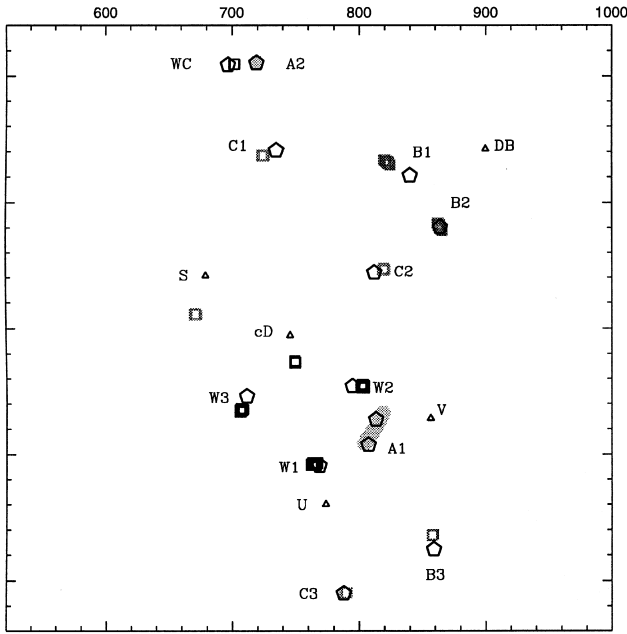
Figure 9. Observed positions for multiple images (hexagons) versus prediction (hatched regions) using the mean sources defined in equation (18). The best-fitting model MIa was obtained using only the positions of the image system A, W and C and considering only the light deflection caused by the cD and the cluster as 'free' parameters. For more details, see text. To check the hypothesis that B3 is the counterimage of B1 and B2, we have inserted the additional images predicted for B2 assuming its redshift coincides with that of cB58.

Figure 10. For the model MIb we used the arc positions Â11 and Â12 instead of A11 and A12. The remaining observables and the lens modelling are the same as for MIa. The arc becomes straighter (but also too long) and the W-system fit improves. We calculated the mean source of B1 and B2 and added the predicted images of that source. As before, the prediction is different from the observation by more than the extent of the galaxies B1–B3. However, it is obvious that B1 and B2 belong to a three-image system, and that the third image is very close to the observed B3.

5.2 Results

The models explored followed a strategy of increasing complexity, aiming at assessing the robustness of the lensing predictions. The first models we investigated used the positions of A1/A2 and B1/B2 as observables; good fits predict that C1/C2/C3 and W1/W2/WC are multiple images; the exact position of W3 depends on the slope of the mass profile in the centre. As W3 has the same 'tail' (in colour and morphology) as W1, W2 and WC with reversed parity relative to W1, it is obviously a fourth image of WC, and it is used for further constraining the mass distribution in the core of MS 1512 + 36. The observations show some evidence that the fifth image is merging 'head on head' with the fourth image (see Fig. 6). If this is the case, then the radial critical line of the combined mass distribution (cluster and cD galaxy) passes through the head of W3. Alternatively, a slightly different redshift for A and W is sufficient to allow an additional image of A (the existence of which is predicted for some of the models) to lie next to the head of W3. We therefore leave the fifth image position of the W system unconstrained. As the galaxy B3 is too faint for a precise measurement of its magnitude in *R*, and on the other hand is surprisingly bright relative to B1 and B2 (which are near a critical line and thus should be magnified considerably), we cannot be absolutely sure that B3 is indeed the counterimage of B1 and B2. Consequently, we use as a first step only the positions of A1/A2, W1/W2/WC/W3 and C1/C2/C3 in the models MIa and b. In a second step
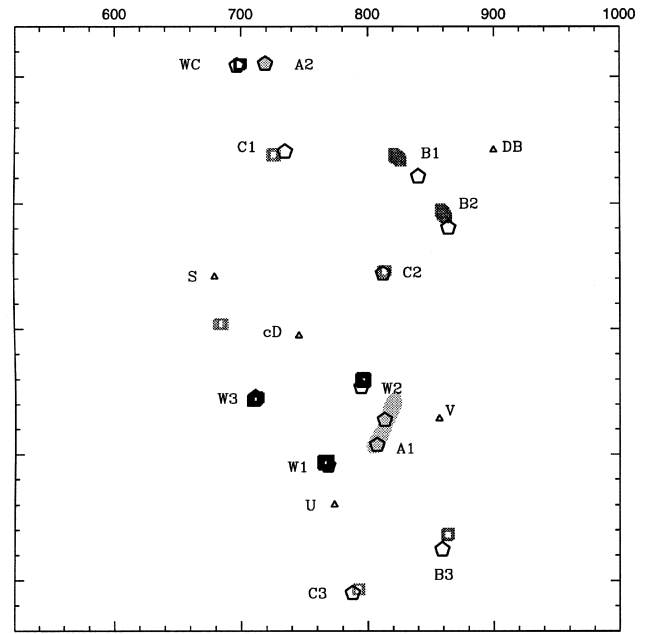
(model MIIa), we reverse the approach and check what happens when the positions of A1/A2. W1/W2/WC/W3 and B1/ B2/ B3 are used. In models MIIIa and MIVa we explore the role of the slope of the potential. For the models MVa, b, and c all the positions are used.

With model MIa we investigate whether it is sufficient to describe the lens system with the deflection potential of the cD, the cluster and DB, and whether models can be found in which the potential depth of the cD galaxy is in agreement with its observed velocity dispersion. Hence the velocity dispersion of the cD is restricted to $246 \text{ km s}^{-1} \leq \sigma_{cD} \leq 306$ km s^{-1} (the 1σ interval for the uncorrected and aperture-corrected velocity dispersion). The ellipticities of the cluster and cD potential are assumed to be smaller than 0.25 and 0.2, respectively; the velocity dispersion of DB is kept constant at $\sigma_{DB} = 84 \text{ km s}^{-1}$. The resulting best-fitting parameters are summarized in Table 2, and the predicted images of the mean sources can be seen in Fig. 9. The arc is curved a little too strongly, but the position of the arc and its counterimage are fitted perfectly. From Fig. 10 and Table 3 we infer that the positions of the predicted images of W (C) are off from the observed ones by 6.7 (6.9) pixels on average and thus the error is smaller than the typical extent ($\gtrsim 10$ pixel) of the images. To see whether B3 is indeed the counterimage of B2 and B1, we mapped the image B2 back into the source plane (assuming its redshift agrees with that of cB58) and we added the predicted images of that source in Fig. 9 as well. As the positions of B1 and B2 were not used for the model fit, one cannot expect that the predicted

position of B1 will agree with that of the observed one. The fact that the predicted third image of B is so close to that of the 'candidate' B3 adds further weight to the hypothesis that B3 is the counterimage of B1 and B2.

To check the robustness of the best-fitting parameters we used the innermost two knots of cB58 (see Fig. 3, where they are marked as $\hat{A}11$ and $\hat{A}12$) instead of A11 and A12 for the fit. The resulting model is called MIb. The two knots together with the reversed parity at A11 and A12 constrain the critical curve at cB58 more strongly, because now the critical line must not only be somewhere between A11 and A12 but more confined between $\hat{A}11$ and $\hat{A}12$. The quality of the fit improves: the fit for the W and A system is almost perfect; the arc becomes straight because of the increased ellipticity ($\epsilon_{cD} = 0.199$) of the cD galaxy. The best-fitting parameters of MIa and MIb differ and they demonstrate that an increase of the velocity dispersion from ≈ 570 to 630 km s^{-1} can be compensated for by an increase of the core radius from 6 to 9 arcsec (which flattens the mass profile in the centre). As far as the arc position and direction are concerned, a more circular cluster profile can be compensated for by an increase of the ellipticity of the deflection potential of the cD galaxy.

We point out that taking into account flux ratios of multiple images cannot resolve this ambiguity: objects near the critical line (B1, B2, A1) cannot be considered, because their flux ratio depends on the details of the mass distribution near the critical line and they cannot be treated as point sources. Thus, only for the objects C1, C2, C3, W1, W2 and WC can one compare directly the magnification ratios predicted by the model with the observed flux ratios. From these objects, the magnitudes of W2 and C2 are affected by red light and absorption in V caused by the cD galaxy (or by inaccurate subtraction of the cD light); because C1 and C3 differ in colour by about 0.6, only W1 and WC remain as 'clean' sources. In the coadded data (which improve the signal-to-noise ratio, especially for WC) we obtain a magnitude difference of $\Delta^W_{C1} = 2.2 \pm 0.75$ for the objects WC and W1. The comparison of the predicted magnitude difference of the multiple images Δ^C_{21}, Δ^C_{31} and Δ^W_{C1} in Table 3 shows that the predicted flux *ratios* are similar and agree reasonably well with the observations, where again MIb is a slightly better fit. The magnification of A2 increases from 2.15 to 2.89 if one changes the parameters from MIa to MIb, because then the larger velocity dispersion provides a larger surface mass density (and shear) at A2.

As the models MIa and b predict the counterimages of B1 and B2 very close to B3, we now use the same observables as for MIa and assume further that B1, B2 and B3 have a common source; the free parameters are as in MIb. The resulting best fit is denoted by MIIa. The quality of the fit is good (see Table 3 and Fig. 11). The C system is predicted very accurately if we use the value for $d_C \approx 1.03$ derived from MIa and b. Of course, a zero velocity dispersion for DB is unrealistic. It is not unexpected, however, that the best-fitting value for the velocity dispersion differs from a reasonable one (say 84 km s^{-1}) because DB is relatively far away from the citical line. For a velocity dispersion of 84 km s^{-1} the shear (and surface mass density) from DB at B1/B2 is only about 0.02. One cannot expect that describing the true deflection potential by the sum of two elliptical potentials provides an accurate fit not only for the observables in

the core but also at the positions of B1 and B2 at the 2 per cent level, because the ellipticity and the slope of the surface mass density are expected to change between the inner and outer parts of the cluster. We have tested how large the deviation from the model potential must be to allow for a perfect fit for the positions of B1, B2 and B3, by applying the same model fit as in the case of MIIa, but now allowing for a 'negative' mass at DB. A 'negative' mass corresponding to -70 km s^{-1} changes the shear and magnification locally by only 0.04 (relative to the $+84$ km s^{-1} case), which is unmeasurable by weak lensing methods, improves the fit quality to $\Delta^2_B = 9$ relative to MIIa and dims the brightness of B1 and B2 relative to B3.

When the positions of the As, Ws and Cs are used for the model fit, the prediction for B is not as good as when the positions of the As, Ws and Bs are used to predict the Cs. The reason is that in the first case the mass profile is probed mainly in the central region, whereas in the latter case the larger distances of B1/B2/B3 allow us to constrain the slope of the mass profile better. We demonstrate this with the model MIIIa, which was derived in two steps. Best-fitting values for the parameters describing the cD galaxy, the cluster and the redshifts were obtained as for MIb, but with a triple weight for the positions of C1, C2 and C3. Using these parameters, the velocity dispersion of DB and redshift of B were varied to optimize the predicted positions for the Bs as well. The best-fitting values are $d_B = 1.02$ and $\sigma_{DB} = 72$ km s^{-1}. As expected (see Table 3), the quality of fit improves in the outer regions and decreases in the core.

Thus we have demonstrated that the numerous multiple images can be fitted at the same time with a very simple model consisting of a singular (non-singular) elliptical
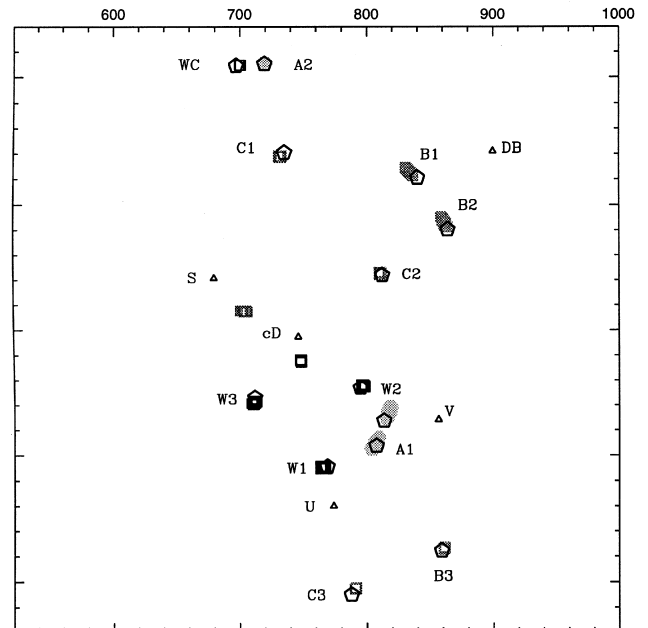

Figure 11. For this fit the free parameters of the lens model were the same as for MIa and b with an additional variation of the velocity dispersion of DB. Instead of the C system, the B system was used for the fit. Assuming that $d_C = 1.03$, the mean source of C1, C2 and C3 is obtained and the predicted images of that source are also plotted.

potential for the cD galaxy (and the cluster). The fact that the best-fitting parameters in Table 2 can be quite different from model to model shows that no fine tuning of the parameters is necessary to explain the multiple images. (However, model MIa and b is not a good fit for the image positions of the B system.) The C images are most robust with respect to a change of the parameters, whereas the W and A galaxies are sensitive to the steepness and height of the combined potential (of course the contributions coming from the cD and the cluster can be varied), and the Bs are more sensitive to the ellpticity and slope of the potential at $\theta \gtrsim 10$ arcsec.

5.3 The magnification of A2 and limits to the velocity dispersion and core radius of the cluster

As not necessarily the whole source of cB58 has to be lensed into the gravitational arc cB58, and the magnification near critical lines is very model-dependent, the magnitude of the unlensed source of cB58 can be obtained most accurately from the counterimage A2.

The most pessimistic statement concerning the magnification of A2 is obtained by considering the so-called mass-sheet degeneracy (e.g. Schneider & Seitz 1995), which states that all dimensionless observables (source separation and flux ratios of multiple images) are invariant under a transformation of the deflection potential according to

$$\psi_{tot}(x, y) \rightarrow \lambda\psi_{tot}(x, y) + (1 - \lambda)(x^2 + y^2)/2; \qquad (7)$$

in other words, a potential cannot be disentangled from a rescaled deflection potential (and thus a rescaled surface mass density and shear) and the addition of a constant-mass sheet with $\kappa_0 = 1 - \lambda$; the constant λ is limited by the fact that the total surface mass density must not be negative.

From the ground-based data of Gioia & Luppino (1994) we infer that the cluster is optically poor and confined to a small region; there is no hint that it is embedded in a larger scale structure that could provide the unconstrained mass sheet. Thus the ignorance about the mass-sheet degeneracy will add only a small uncertainty for the magnification of A2 relative to the unlensed source.

The unconstrained core radius of the cluster, however, can mimic the mass-sheet degeneracy locally: increasing the velocity dispersion and the core radius of the cluster is similar to rescaling the potential and adding a constant surface mass density, as long as only a few positions (those of the multiple images) are considered and these positions are not spread enough in radius. If only the A and W systems are taken into account in the model fit, a large cluster velocity dispersion cannot be excluded, because then one can increase the core radius to suppress the central mass peak; for a velocity dispersion of $\sigma_{cl} = 840$ km s^{-1} one obtains a best-fitting core radius of about 20 arcsec and $\sigma_{cD} = 278$ km s^{-1} with a fit quality of $\Delta_W^2 \approx 300$ and $\Delta_A^2 = 2$. The magnification of A2 is then approximately 7. Even if one ignores the B and C systems, a model demanding such a large core radius seems to be implausible. On the other hand, if one uses only the positions A11, A12, A2 and W1, W2, WC and W3, with limits for σ_{cl}, $\epsilon_{cl, cD}$ as in the previous models, and does not restrict the velocity dispersion of the cluster, low values for its velocity dispersion and core radius are favoured (the corresponding best-fitting values are sum-

marized as MIVa in Table 2 and illustrated in Fig. 12). The magnification of A2 agrees with that obtained for earlier models in Table 3.

Including the positions of the B system must constrain the maximum velocity dispersion most strongly. For a conservative estimate we ignore the fact that B3 is most likely the third image to B1 and B2. In this case, an increase of the lensing strength for B1 and B2 for large velocity dispersions can be avoided by shifting them to lower redshift. Without a lower limit for the velocity dispersion of the cD, i.e. allowing for a redistribution of mass from the cD to the cluster and with restrictions for the remaining parameters as for model MIIa, we obtain a maximal acceptable velocity dispersion of the cluster of $\sigma_{cl} = 670$ km s^{-1}, with a core radius of ≈ 11.2 arcsec and a cD velocity dispersion of 250.8 km s^{-1}. The relative lensing strength of B then has to be $d_B \approx 0.9$, corresponding to a redshift of 1.7 in an Einstein–de Sitter universe. For this maximal velocity dispersion the magnification of A2 is equal to $\mu_{A2} = 3.4$. If B3 is the counterimage of B1 and B2, the maximal acceptable velocity dispersion has to be as low as 600–610 km s^{-1} to obtain a marginal fit with $\Delta_B^2 \leq 550$. Note that MIb cannot be considered as a good fit for B1, B2 and B3 and that in this case the sum in Table 3 includes only the positions of B1 and B2. For a cluster velocity dispersion of 600 km s^{-1} the velocity dispersion of the cD and the core radius become 257.8 km s^{-1} and 8.8 arcsec, respectively. The magnification of A2 equals 2.56 in this case.

These investigations show that in fact the magnification of A2 is limited by $2.0 \lesssim \mu_{A2} \lesssim 3.4$ if B1, B2 are considered
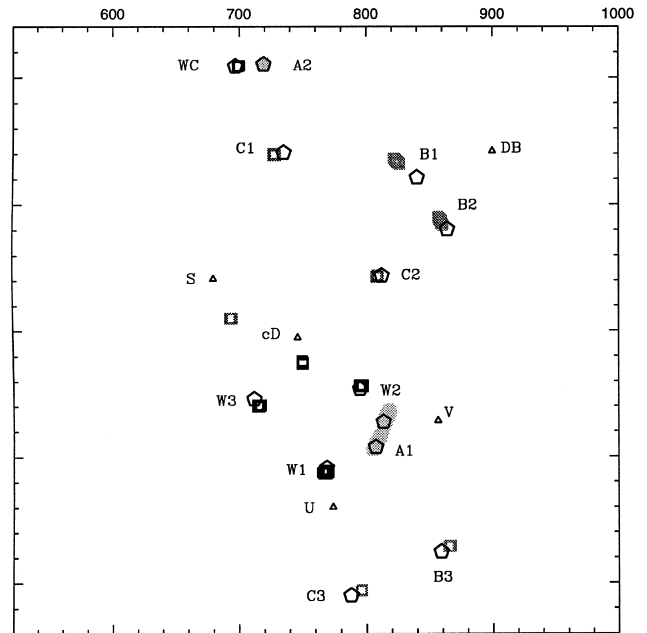

Figure 12. For model MIVa we used only the positions of the A and W systems to constrain the parameters describing the cD galaxy and the cluster. The allowed range of parameters was limited by $\epsilon_{cD} \leq 0.2$, $\epsilon_{cl} \leq 0.25$ and $246 \leq \epsilon_{cl} \leq 306$ km s^{-1}. The cluster velocity dispersion was not limited. The multiple image positions for the C and B systems are predicted under the assumption $\sigma_{DB} = 84$ km s^{-1}, $d_B - 1.02$ and $d_C = 1.035$.

and by even more $(2.0 \lesssim \mu_{A2} \lesssim 2.9)^2$ if B3 is the third image of B1 and B2. Concerning the possible velocity dispersions of the cluser, the best-fitting parameters for the models MIa and MIb are almost as different as they can be to allow a good fit. We have tested this by giving different weights to different multiple image systems, considering B1/B2/B3 instead of C1/C2/C3, demanding that the ellipticity and orientation of the cD potential equals that inferred from the light, taking into account the galaxies V and S as possible deflectors, etc. From this we infer limits of 540 km s$^{-1} \leq \sigma_{cl} \leq 670$ km s^{-1}, 5.5 arcsec $\leq \theta_{cl}$ 11 arcsec and $6° \leq \phi_{cl} \leq 14°$. Of course, these limits weaken if one uses only the positions of the A or W system for the fit.

5.4 Alignment of cD light, cD potential and the cluster potential

In the models MI–IV the ellipticity and orientation of the cD potential were treated as free parameters. The best values for the ellipticity and orientation for those models are spread between 0–0.2 and $\approx 11°$–$19°$. This does not imply that the ellipticity and major axis of the cD potential is inconsistent with the values inferred from the light using Fig. 2 and the relation $\epsilon_{cl} = 3\epsilon_{cl}$. As lensing is only sensitive to the combined potential of the cD and the cluster, the orientation and ellipticity of the *individual* potentials are undertermined within some range (see Table 2). To demonstrate the consistency of the cD potential with the light distribution of the cD, we kept the cD parameters $\epsilon_{cD} = 0.06$ and $\phi_{cD} = 10°$ fixed, varied those describing the cluster, the velocity dispersion of the cD ($246 \leq \sigma_{cD} \leq 306$ km s^{-1}) and DB ($70 \leq \sigma_{DB} \leq 100$ km s^{-1}), and the redshifts of the W, C and B systems. We used the positions of the A, W, B and C systems for the fit. With the exception of the B positions, the best-fitting model (MVa) recovers the multiple image positions very well. When $\epsilon_{cD} = 0.11$ is assumed (model MBv) the fit quality reduces. For MVa and b the major axes of the potentials of the cD and the cluster are almost parallel. As a consequence, the fit quality stays comparable to the models MVa and b, if one requires that the cD potential is strictly parallel to that of the cluster: we obtain $\phi_{cD} \equiv \phi_{cl} \approx 12°$ (see model MVc in Table 2). For the models MVa and b the weights $w(i_k)$ in equation (1) were equal for all positions used for the fit. As the multiple image positions are concentrated in the cluster core (W1, W2, W3, A11, A12), the mass profile is constrained most strongly there, and these observables are reproduced with the largest accuracy. Giving a weight of 2–3 to the positions of the C system (B system) and fitting the parameters in analogy to MVc, the accuracy for the prediction of the C *and* B (B *and* C) systems increases. This adds further weight to the hypothesis that both the C and B systems are triple image systems. With the large weight of the outer multiple images, the orientation of the major axis of the cluster and cD potential decreases to 10° and 9°. This tilt of the major axis of the potential is also seen in the light of the halo of the cD galaxy: for $\theta \leq 5$ arcsec (A and W system) the position angle equals about 10° and

drops to $\leq 8°$ in that region where the images C and B occur ($\theta \leq 7.5$ arcsec).

We conclude that the cD and the cluster are aligned and have a major axis position angle of about 10°, the ellipticity of the combined potential increases and the position angle of the major axis changes in the outer parts of the cluster. The orientation of the major axis of the optical light and the dark mass thus agrees with that of the X-ray light found by Hamana et al. (1997).

6 THE MAGNIFICATION OF THE ARC

Up to now only two spots (A11 and A12) of the arc have been used for the lens modelling, and they were treated as positions of multiple images. To make more use of the two-dimensional light distribution of the arc for the lens modelling, we consider only (CCD) pixels where the counts exceed a rate of 5.5 and subdivide each pixel into two triangles (see Schneider, Ehlers & Falco 1992, p. 300). For each model p, all triangles of the arc are mapped into the source plane. Using a ≈ 50 times denser grid than in the lens plane, we identify for every triangle in the image plane all grid points in the source plane that lie within the corresponding triangle in the source plane. For a perfect model, each grid point in the source plane is contained either in no or two triangels. In the second case one of these triangles has positive parity with respect to its correpronsing triangle in the image plane (which is outside the critical line), and the other is mapped with negative parity on to the image plane (and the corresponding triangle is inside the critical line). Within the accuracy given by the finite spatial resolution of the CCD pixels, the surface brightness of such triangles should also agree. Gridpoints in the source plane that are singly imaged only reflect an imperfect model (and observational errors). To obtain a model that predicts the correct shape of the arc, we thus add a term proportional to

$$\eta = \frac{N_s - N_d}{N_s + N_d} \qquad (8)$$

to equation (1), where N_s and N_d are the number of grid-points in the source plane that are singly and doubly imaged, respectively. Note that adding a term proportional to N_s or $-N_d$ instead of equation (8) would introduce a bias towards high and low magnification of the arc. The value of equation (8) is independent of the magnification of the arc and equals ($+1$) and (-1) for a bad and an optimal model, respectively. The best-fitting parameters are obtained in two steps: first the positions of the multiple images are used for the model fit and then the arc-shape constraints (8) is added to equation (1) and the minimization is continued. Whereas we generally use three positions (A11, A12, A2) to fix the arc and its counterimage, we consider only A11/A2 or A12/A2 when the shape is taken into account. This guarantees on the one hand that the global properties of the lens are changed only slightly, and in particular that the counter-image stays at the same position; on the other hand, it allows changes in the mass distribution to turn the arc in the correct direction. In Section 5 we showed that a good fit for the multiple image systems can be obtained by combining the deflection potential of the cluster and the cD galaxy.

---

[2] These limits were not derived from a rigorous investigation, but contain all magnifications for A2 predicted by models that include B3 in their fit.

This is not the case for the arc shape: we cannot obtain a good fit for the arc shape *and* the position of the W and A systems at the same time, because the arc demands a lot of shear parallel to its major axis. A possible reason for the insufficient fit can be inferred from Figs 1 and 3: the arc is not entirely straight but curved, and the centre of curvature points in the opposite direction from that one would expect if it were caused by the cD and the cluster. A possible cause of this curvature is a perturbation of the light deflection by the galaxy V on the right side of cB58. The galaxy V has the same blue colour but a much smaller surface brightness than cB58. Thus it could be a blue, low-surface-brightness galaxy at low redshift or a 'normal' field galaxy at $z > 1$. We consider the first alternative as unlikely because of the small number density of those galaxies. If the redshift of V is ≥ 2, then it lies close to, or on, the critical curve of the lens corresponding to the redshift of V. The 'close' case can be ruled out because there is no 'second' image on the opposite side of the critical line with comparable brightness. the fact that V has a double core on opposite sides of the $z \approx 2.7$ critical curve would favour the 'on the critical line' case. However, in that case a much more elongated object, similar to cB58, would be expected and a counterimage on the right side A2 should be observable. The object 3.4 arcsec to the right of A2 is too far away and has too red a colour to be an option. We conclude that the galaxy V is at a redshift larger than 1, but small enough to avoid being multiply imaged. In this case a two-lens screen situation arises, where the light of cB58 is distorted by the galaxy V before it is deflected by the cluster. As we do not know the redshift of V, we treat the light deflection as if it takes place at the redshift of the cluster and model V as a singular isothermal sphere. The best-fitting velocity dispersion σ_V cannot then be easily related to the depth of its potential, but describes only the 'effective' lensing strength of this galaxy. A two-screen model will only be useful once the redshift of V is known. Most generally, the velocity dispersion σ_V can be considered as a one-parameter correction for the effective shear and surface mass density at the arc.

For completeness we now also take into account the light deflection caused by the spiral S. This is done to show that the additional light deflection of the spiral does not change our preceding conclusions, i.e. that the multiple image positions are in agreement with the expectations from optical and X-ray light and the dynamical properties of the cluster galaxies. As none of the multiple images is close to the spiral, it adds only a small perturbation to their total deflection. Irrespective of its exact redshift ($z_S \approx 0.3$) we can therefore approximately describe its light deflection as taking place at the redshift of the cluster. We assume that the depth of its potential does not exceed 180 km s^{-1}, which corresponds to the three-dimensional velocity dispersion of a 1.8-L_* galaxy.

Fig. 13 shows the reconstructed sources for the arc cB58. It was obtained using the arc shape (as observed), and the A, B, C and W system with a low weight for the B positions. The value of η defined in equation (8) equals -0.62, and the remaining numbers characterizing the fit quality for the positions are shown in Table 3 (model MVIa). The area of the arc in the source plane equals 3.62–4.46 (dithered) pixels, where the range is obtained from either considering only the doubly imaged source pixels or all pixels in the

source plane. This size is in agreement with that of the counterimage A2 (16 pixels) if one takes into account that A2 is magnified by a factor of 2.4 and if about half of the total source is lensed into the gravitational arc cB58 (as is indicated in Fig. 13 as well). From the size ratios of the arc source (3.61–4.46 pixels) and the non-deconvolved arc (213 pixels) we obtain a magnification factor of $\mu_{\mathrm{arc}} \approx 47.8$–59.0 within the contour of 5.5 count pixel^{-1}. In Fig. 13 we have also unlensed the shape of A2 using the predicted surface density and shear of the model MVIa at the position A2. On the surface brightness contours of the unlensed object A2 we have overlaid those of the reconstructed source of cB58. The contours of 5.5 count pixel^{-1} agree very well, although only the shape and not the flux distribution of the arc were used for the model fit. The contour at 10 count pixel^{-1} is a little larger for the reconstructed arc source than for the unlensed counterimage. These differences can be attributed to the finite pixel size in the image of A2. Fitting the shape of the arc adds only a local constraint to the model and does not break the velocity dispersion–core radius degeneracy discussed before. Thus the total magnification of the arc will also increase if the velocity dispersion and core radius are increased. The corresponding magnification of the arc can, however, be estimated from the magnification of the counterimage: using the facts that the sizes of the arc and A2 are 213 and 16 pixels within the 5.5 count pixel^{-1} contour and that only a fraction $f \approx 1/2$ of the total source is imaged into the arc cB58, one can roughly estimate the arc magnification to be $\mu_{\mathrm{arc}} \approx 213/16\ \mu_{\mathrm{A2}}/f \approx 25\ \mu_{\mathrm{A2}}$.

In Fig. 14 the gravitational shear field, surface mass density and magnification contours are plotted for the model MVIa. The shear field is a measure for the direction and ellipticity that a circular source obtains through the lens effect of the combined mass distribution at the same position. One can see that the shear field left of the elliptical E
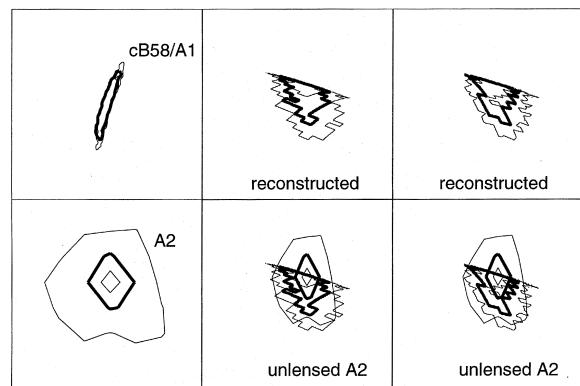

Figure 13. In all six panels we plot surface-brightness contours of 5.5, 10 (thick contour) and 15 count pixel^{-1}. The upper left panel has a sidelength of 5 arcsec and shows the surface-brightness distribution of cB58. The remaining squares are 0.35 arcsec on a side. The upper middle and upper right panels show the reconstructed source (model MVIa) using the negative parity and positive parity parts of the arc, respectively. In the lower left panels the contours of the counterimage A2 can be seen. Using the surface density and shear at the position of A2 we 'unlens' the shape of A2 and obtain the squeezed contours in the lower middle and right panels. On top of that the corresponding contours of the reconstructed source of the arc are overlaid.
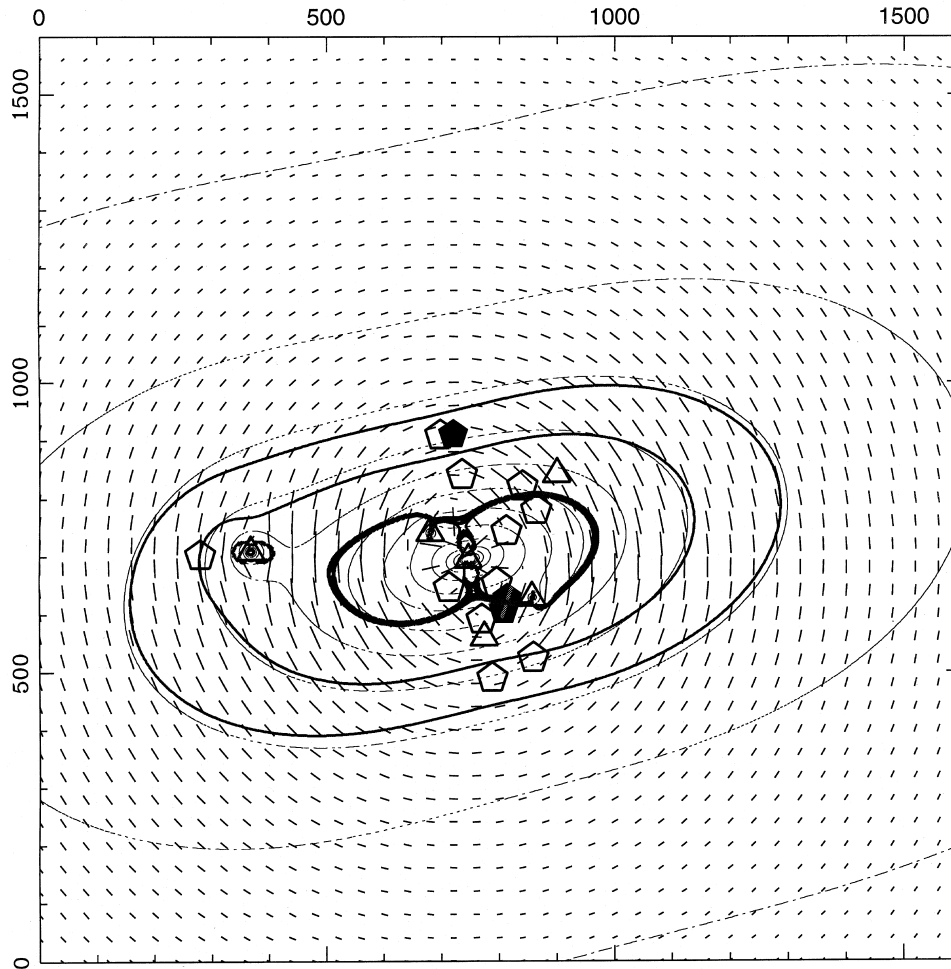
Figure 14. Shear field (vectors), surface density contours (dotted lines) and magnification contours (solid lines) for sources at redshift 2.7 according to the model MVIa. The surface density contours start at $\kappa = 0.1$ and are spaced by 0.1. Filled (empty) pentagons denote the positions of A11/A12.A2 (and the remaining multiply imaged galaxies). Other galaxies like the cD, the spiral, the elliptical E and the perturbers DB and V are added as empty triangles. The three thick contours are those of magnification 2, 3 and 'infinity' and thus the central thick contours denote the critical lines for a galaxy at redshift 2.7.

is parallel to the y direction of the chip, and thus explains the large distortion of the arclet left of E (its magnification equals 3 for a redshift similar to cB58). The surface density contours start at $\kappa = 0.1$ and are separated by $\Delta\kappa = 0.1$. Using an elliptical potential provides elliptical isodensity contours only for small values of ϵ. For large eccentricities the isodensity contours become 'peanut-shaped'. Only the outermost density contours ($\kappa = 0.1$–0.2) suffer slightly from this unrealistic simplification. In these regions, the exact mass distribution is not well constrained by the strong lensing effect anyway. However, independent of the details of the lensing model, the mean surface density in the chip 3 is $\langle \kappa \rangle \approx 0.2$. The thick contour are those of magnification 2, 3 and infinity (critical line for a source at $z = 2.7$).

7 WEAK LENSING ANALYSIS

We next consider the distortion of images of (presumably background) galaxies near the core of MS 1512. With this analysis we do not aim at a weak lensing mass reconstruction as in the case of Cl0939 + 4713 (Steitz et al. 1996) – where the observations were deeper and the lens stronger –

but at a consistency check of the wek lensing signal with the cluster parameters estimated from multiple images. We use the coadded V and R data and consider only galaxies in the WFPC fields, which are within a distance of 80 to 850 pixels (i.e. within a distance of 42.5 arcsec) from the centre of light of the cD galaxy. The outer radius equals the maximum radius of a circular disc centred on the cD galaxy that is completely within the data region. A size cut of 50 (dithered) pixels is applied, and stars and objects with a SEX-TRACTOR flag larger than 16 are excluded. This excludes objects with incomplete or corrupted aperture or isophotal data.

The minimum flux of galaxies considered for the weak lensing analysis was set equal to that of the completeness limit of the number counts in the $V + R$ data. The bright cut-off was set at 2.5 times this limiting flux. Comparing the number counts for these galaxies in the WFPC2 field with published results on the I-band counts (Smail et al. 1995), we estimate that the selected galaxies have I-band magnitudes of about $23.3 \lesssim m_I \lesssim 24.3$. According to the evaluation of the CFR Survey (Lilly et al. 1995), the mean redshift of those galaxies is predicted to be of order 1.

The shapes of the galaxies are estimated with the SEXTRACTOR software package (Bertin & Arnouts 1996). The width σ_χ of the ellipticity distribution of the remaining 33 (29 of them are within chip 3) galaxies is estimated and it is assumed (and checked) that this width is basically unaffected by lensing. The deflection potential of the cluster is described by equation (1), with the ellipticity, orientation and velocity dispersion as free parameters, and the core radius is assumed to be equal to 7.5 arcsec. Let χ_i be the complex ellipticity as defined, e.g., Schneider & Seitz (1995), of the ith object, and $\langle\chi\rangle_i(\boldsymbol{p})$ the model-dependent expectation value at the same position; further let $\sigma_\chi t_i(\boldsymbol{p})$ [for details on $t_i(\boldsymbol{p})$ see also Schneider & Seitz 1995] be the width of the ellipticity distribution expected at the position of the ith object for lensing parameters $\boldsymbol{p}$; we then minimize

$$F := -\sum_{i=1}^{n_{gal}} \ln \left\{ (1-f_{cl}) \frac{1}{t_i^2(\boldsymbol{p})} \exp\left[\frac{-|\chi_i - \langle\chi\rangle_i(\boldsymbol{p})|^2}{\sigma_\chi^2 t_i^2(\boldsymbol{p})} \right] \right.$$

$$\left. + f_{cl} \exp\left[-\frac{|\chi_i|^2}{\sigma_\lambda^2} \right] \right\} \tag{9}$$

with respect to $\boldsymbol{p}$; for the contamination of the galaxy sample with cluster members (or foreground galaxies) we assume $f_{cl} = 0.1$. To parametrize the distance to the galaxies we assume, in analogy to equations (2)–(4), a relative lensing strength of $d = 0.72$, which corresponds to a mean redshift of $\langle z \rangle \approx 1$ in an Einstein–de Sitter universe. For 1000 bootstrapping realizations of the data catalogue we determine the best-fitting parameters for the velocity dispersion, the major axis position angle and the ellipticity of the deflection potential of the clusters. The result is shown in Fig. 15, where each point in the ϵ_{cl}–σ_{cl} and ϕ_{cl}–σ_{cl} planes corresponds to a best fit for one bootstrapped data catalogue. We added contours in which approximately 90 and 68 per cent of the best-fitting parameters are contained. According to Fig. 15, the 1σ interval for the velocity dispersion and the major axis position angle equals [520, 670] km s^{-1} and [5°, 50°], with best-fitting values of about 600 km s^{-1} and 20°. We point out that the estimate for the velocity dispersion depends on the mean redshift assumed for the galaxies and on f_{cl}. If the former was equal to 0.8 instead of 1, the estimated velocities increase by 10 per cent. Another uncertainty is the unknown core radius, because the data field (42 arcsec radius) is not very large compared with the core
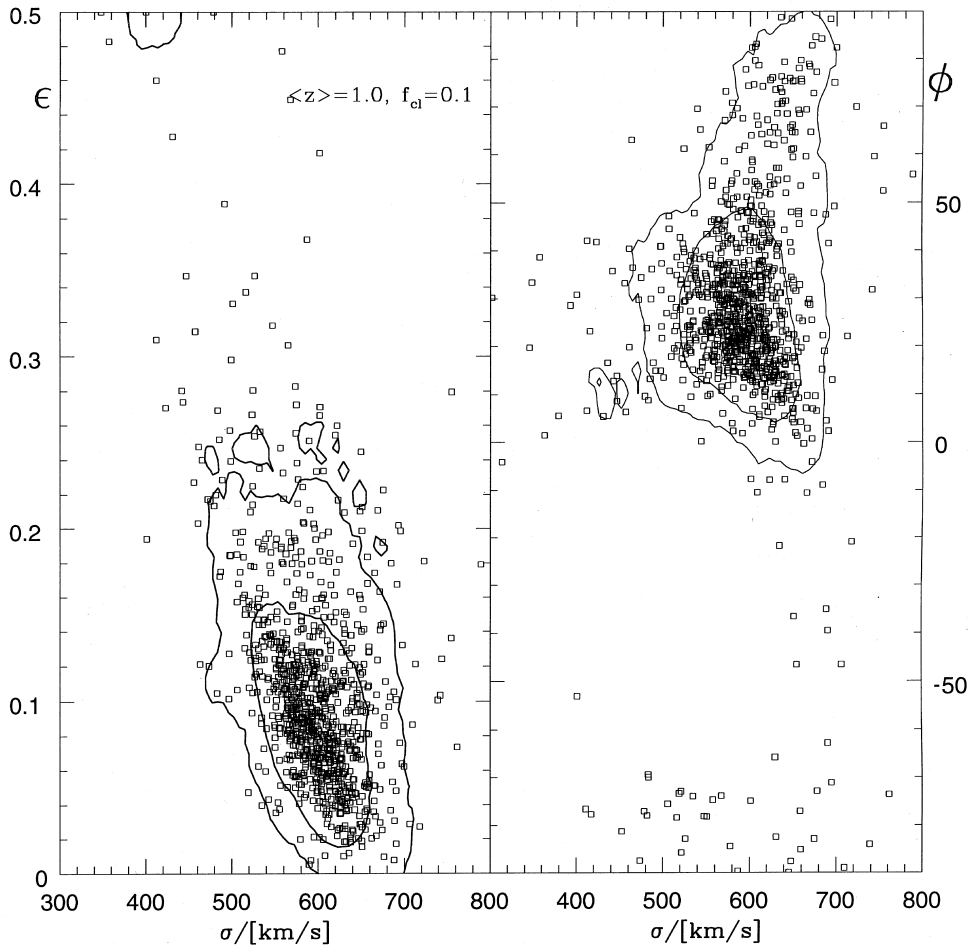

Figure 15 Best-fitting estimates for the velocity dispersion, ellipticity and major axis position angle of the cluster using 1000 bootstrapped realizations of galaxies with $24 \leq m_{V+R} \leq 25$ within ≈ 42 arcsec distance of the cD galaxy. The contours approximately indicate that region in which 68 and 90 per cent of the best-fitting values are contained. The mean redshift of the galaxies and the contamination with cluster members were assumed to be $\langle z \rangle \approx 1.0$ and $f_{cl} = 0.1$.

radius. If the core radius is allowed to vary between 6 and 10 arcsec, the distribution of the points in the $\epsilon - \sigma_{cl}$ plane becomes broader, in particular towards larger velocity dispersions, because a larger core radius can be compensated for by an increased velocity dispersion. But even in this case, both the 68 and 90 per cent upper confidence limits for the velocity dispersion are still below 800 km s^{-1}. The assumption of a core radius of 7.5 arcsec is, by the way, not unreasonable because it agrees with that found from the X-ray observations of this cluster (Hamana et al. 1997).

8 SUMMARY AND DISCUSSION

We have shown that the 'protogalaxy' cB58 owes its large apparent brightness to the lens effect caused by the cluster MS 1512 and its cD galaxy. The symmetry in the surface-brightness distribution reveals that cB58 is a gravitational fold arc; the large axis ratio is caused by the stretching of the source parallel to the major axis of the arc.

Three systems of multiply imaged galaxies are found. In the first case (W), a shrimp-like object is mapped into five images, of which four can be identified. The redshift of the W system must be very similar to that of cB58. Measuring the flux ratios and colours of the galaxies of the W system is difficult, because all objects are small, not much above the noise level, and their colours are affected by red light and absorption caused by the cD galaxy.

The second system (C) consists of three images which also have poorly determined and slightly inconsistent colours. The three images of the system have the same head–tail morphology, their positions can be fitted robustly for different parameters of the lens models, and the relative inclinations of their head–tail axes agree with the predictions from lens models. For most models the source redshift is $z \approx 3.5$.

The third system (B) is also a triple system; two images are close to the tangential critical line and their magnification is affected by a nearly elliptical galaxy (DB) with an estimated velocity dispersion of $\sigma_{DB} = 84$ km s^{-1}. The estimated redshift of the source is ≈ 3. However, a precise prediction for the redshifts of the B and C systems is difficult, because the lensing strength increases only slowly with redshift (see Fig. 8) and thus a broad range of redshifts is formally possible. An upper limit of $z < 4$ for the B and C systems is set by their detectability in the *B*-band observations of Gioia & Luppino (1994).

The lens system was modelled with a singular (non-singular), elliptical, isothermal potential for the cD galaxy (for the cluster) and isothermal potentials for additional galaxies. Because the multiple images are not spread much in radius, a core radius–velocity dispersion degeneracy arises; if only the inner image systems (W and A) are considered, a cluster velocity dispersion of 840 km s^{-1} cannot be excluded if a core radius as large as ≈ 20 arcsec is accepted. Without any restriction on the cluster velocity dispersion, lower values for σ_{cl} and ζ_{cl} are favoured. Giving equal weight to all multiply imaged objects, the inner multiple image systems are fitted better than the outer ones, because a high weight is given to the central mass profile. With an increased weight for the outer images, the outer positions can be fitted better, at the cost of the central images. This is

expected because we have more observables (12 image positions = 24 observables) and up to 11–13 free parameters (four for the cluster, three for the cD, one for DB, three for the redshifts of the W, C and B system, possibly also one for V and S) and one cannot expect the true mass distribution to follow the model in every detail. Most likely, there is a change of the ellipticity and orientation of the cluster potential with radius, as is visible in the cD light and the X-ray contours.

The best-fitting cluster velocity dispersions are of the order of 600 km s^{-1} and thus are at the low end of the dynamical estimates of Carlberg et al. (1996a,b). However, the amplitude $\psi_0 \propto \sigma_{cl}^2$ determined by the lens modelling can be easily related to the 'real' dynamical velocity dispersion only in the spherical symmetric case, where $\sigma_{cl} \equiv \sigma_{dyn}$ should hold. Under the following two assumptions, the weak lensing analysis confirms a low-velocity dispersion σ_{cl} of the cluster. First, we assume that the core radius of the cluster is approxiamtely 7.5 arcsec; this assumption is assisted by the X-ray results of Hamana et al. (1997) [(6.9 ± 1.4) or (7.5 ± 1.5) arcsec, according to the two cases analysed there], which do not normally overestimate the core radius of the dark mass profile. Secondly, we have assumed – after comparing the number counts with those of the *I* band and using the CFRS results – that the mean redshift of the galaxies used for the weak lensing analysis is 1. As the cluster velocity dispersion is in agreement with the value of Carlberg et al. (1996a,b), this is also the case for the total mass estimate and the mass to light ratio of the cluster.

(i) If we consider only the velocity dispersions $\sigma_{cl} \approx 600$ km s^{-1} and $\sigma_{dyn} = (690 \pm 100)$ km s^{-1} derived from lensing and peculiar velocities and ignore the asymmetry for the mass estimate within the virial radius, the lensing mass is 75 per cent of the dynamical mass, but of course compatible to it within the error bars.

(ii) Including all galaxies considered for the light deflection, we obtain (for an Einstein–de Sitter cosmology) a mass within chip 3 of $\approx 8 \times 10^{13} h_{50}^{-1} M_\odot$, which transfers to a mass of $1 \times 10^{15} h_{50}^{-1} M_\odot$ within the virial radius of $1.803 h_{100}^{-1}$ Mpc (Carlberg et al. 1996b), if the combined mass profile of the cluster and its galaxies is isothermal out to the virial radius. The Carlberg et al. (1996a) value is $5.5 \times 10^{14} h_{100}^{-1} M_\odot$ (for $\Omega = 0.2$) and this estimate decreases by about 10 per cent if one uses $\Omega = 1$.

Hamana et al. (1997) suggested using the measured quantities (in their case the X-ray temperature and the core radius MS 1512) to model the lensing of cB58 and to derive limits for the cosmological constant (for flat universes). Although velocity dispersion estimates would drop by ≈ 15 per cent for a flat $\Omega = 0.3$ universe relative to an Einstein–de Sitter universe, we do not consider this as a promising method, because the true mass distribution is only described approximately by two elliptical potentials, and the best-fitting value σ_{cl} cannot straightforwardly be related to the measured σ_{dyn}. A comparison of the relative lensing strengths for the multiple images at different source redshifts will not improve this situation, although these estimates are less model-dependent. The reason is that the lensing strength of a $z = 3.17$ source relative to that of cB58 equals 1.0250, 1.0217 and 1.0195 for an Einstein–de Sitter, a flat $\Omega = 0.3$ and a $\Omega = 0.3$ universe with vanishing cosmo-

logical constant, and thus the fractional differences are in the permille range.

Using imaging and spectroscopy under excellent seeing conditions could further improve the lens models. Deeper photometry in *V* abd *R* or additional filters can show that B3 is the third image corresponding to B1 and B2. If the flux ratios of all the multiply imaged galaxies can be obtained more accurately, they can quantitatively be included into the lens modelling. We consider this as difficult, because then a filter needs to be chosen where the absorption and emission of the cD are small, and where the blue galaxies C and W are bright enough. If the redshift of V (and not so important but much easier, the redshift of S) is determined, a two-screen model can be used. The uncertainty in the lensing strength of B and C (see Table 2) is much larger than the minimum uncertainty given by the unknown cosmological parameters. Therefore redshift measurements of the C and B systems can improve the constraint on the slope and thus the core radius of the potential.

One of the goals of our investigations was to show that cB58 is a fairly 'normal' high-resolution galaxy. This becomes most obvious when the counterimage A2 is considered and its magnification of $\mu_{A2} = 2\text{--}3.5$ is taken into account. Therefore, cB58 is 3.35–4 magnitudes brighter than its unlensed (total) source. If one shifts the data point for cB58 in the magnitude–redshift plane in fig. 5 of Lowenthal et al. (1997) by that amount, one sees that the source of cB58 is a normal '$z = 3$ Steidel galaxy' in the *I*-magnitude–redshift plane. This is also valid for the source size: the half-light radius of A2 is 0.25 ± 0.05 arcsec in the *V* and *R* bands, which equals 3, 3.75 and 1.9 h_{50}^{-1} kpc in a $q_0 = 0.05$, Einstein–de Sitter and flat universe with $\Omega = 0.1$, respectively. The half-light angle agrees with that found by Steidel et al. (1996b) for galaxies of the same redshift. Including the minimum magnification $\mu_{A2} \gtrsim 2$ of A2 decreases the half-light radius by 30 per cent, i.e. to 0.18 arcsec or 2.12 h_{50}^{-1} kpc for $q_0 = 0.5$. Thus the unlensed source A agrees in *R* magnitude, redshift and half-light radius with the galaxy C2-05 in the *HDF* (Steidel et al. 1996b). To compare our investigations with absolute *B*-band luminosities of other high-redshift galaxies (Lowenthal et al. 1997, fig. 6), we avoid the uncertainties related to the k_V correction and simply consider the *H* band, which is approximately equivalent to the rest *B* band at $z = 2.72$. We then correct $m_H = 19.82$ for extinction according to the value $E(B - V) = \times 0.3$ given by Ellingson et al. (1996). The authors found that a 10-Myr-old constant star-formaton model with this amount of extinction provides the best fit to the optical–IR data of the galaxy. Therefore, taking into account the uncertainties in the magnification factor and the extinction correction, the m_H implies a rest-frame *B* absolute magnitude in the range $-25.43 \leq M_B \leq -24.05$ ($H_0 = 75$ km s^{-1} Mpc^{-1}, $q_0 = 0.05$) quite close to the $M_B \simeq -24$ in Lowenthal et al. (1997). An even better agreement is obtained if the lower value $E(B - V) = 0.1$ adopted by Lowenthal et al. (1997) is used.

The enormous size of the flux of cB58 can be attributed to the gravitational lens effect. This is of course not the case for the surface brightness, which is conserved by lensing. As the surface brightness stays high all over cB58 and it is fairly structureless (despite the spots in Fig. 3, which are not visible from the ground), this was interpreted as an indica-

tion for a simultaneous and high star-formation spread over the entire galaxy, and therefore cB58 was denoted a primeval galaxy. The reconstruction of the source of the arc shows that only a part of the source is lensed into cB58, and that those regions with higheset surface brightness experience the largest magnification. The light distribution of cB58 is a 'zoom' into the central part of its source where the star-formation rate is high. The comparison of the spectral properties (line width and ratios) of cB58 and its counter-image will therefore give limits on the inhomogeneity of the star formation in the source of cB58 with unprecedented spatial resolution.

It seems surprising that a 'weak' cluster with a velocity dispersion of $\sigma \approx 600$ km s^{-1} can act as a strong lens, and that not only one but four multiple image systems are found. This can be attributed to the high surface density of $z > 2$ galaxies (Lowenthal et al. 1997) and the increased lensing strength for these sources, compared with $z \approx 1$ galaxies. With the sources A, B, C, W and the arclet lying 12 arcsec north–north-east of the cD (which is similar in colour and surface brightness to B1/B2), we have at least five candidates with a redshift larger than 2 (or 2.5) within a radius of 15 arcsec around the cluster centre, corresponding to a large number density of ≈ 25 galaxies per arcmin². This number density increases when one takes into account that these sources originate from a much smaller area in the source plane and that the slope of the logarithmic number counts at those redshifts is probably not steeper than 0.4. Comparisons with predicted and observed high-redshift number counts are difficult because of the individual magnification of the galaxies and because these investigations use galaxies with a flux limit in the *I* or '*I* + *V*' band. The large number of high-redshift galaxies can also be caused by statistical fluctuations or by a group of galaxies at $z = 2.7$, because we cannot exclude the possibility that the sources of the W and B systems are at the same redshift as cB58. Our investigations show; in addition to those of Franx et al. (1997) and Trager et al. (1997), that the analysis of galaxies lensed by foreground clusters provides a highly successful method of finding high-redshift galaxies.

Finally, we have shown that a cluster with a velocity dispersion as low as $\sigma \approx 600$ km s^{-1} is not only detectable by weak lensing methods, but its velocity dispersion is still measurable within an accuracy of 150 km s^{-1} at a 1σ level. This confirms the claim (Schneider 1996) that even less massive dark matter haloes can be detected at a statistically significant level under the same observing conditions as here, and that haloes of the same depth can be detected in shallower observations with a larger point-spread function.

ACKNOWLEDGMENTS

manuscript. This work was supported by the 'Sonderfor-schungsbereich 375-95 für Astroteilchenphysik' der Deutsche Forschungsgemeinschaft.

REFERENCES

Asada H., 1997, ApJ, 485, 460
Bender R., Möllenhoff C., 1987, A&A, 177, 71
Bender R., Saglia R. P., Ziegler B., Belloni P., Greggio L., Hopp U., Bruzual G., 1998, ApJ, 493, 529
Bertin E., Arnouts S., 1996, A&AS, 117, 393
Bruzual G. A., Charlot S., 1993, ApJ, 405, 538
Carlberg R., Yee H. K. C., Ellingson E., Abraham R., Gravel P., Morris S., Pritchet C. J., 1996a, ApJ, 462, 32
Carlberg R. et al., 1996b, ApJ, 462, 32
Dressler A., Faber S. M., Burstein D., Davies R. L., Lynden-Bell D., Terlevich R. J., Wegner G., 1987, ApJ, 313, L37
Ebbels T. M. D., Le Borgne J. F., Pello R., Ellis R. S., Kneib J.-P., Smail I., Sanaahuja B., 1996, MNRAS, 281, L75
Ellingson E., Yee H. K. C., Bechtold J., Elston R., 1996, ApJ, 466, L71
Franx M., Illingworth G. D., Kelson D. D., van Dokkum P. G., Tran K.-V., 1997, ApJ, 486, L75
Fukugita M., Futamase T., Kasai M., Turner E. L., 1992, ApJ, 393, 3
Gioia I. M., Luppino G. A., 1994, ApJS, 94, 583
Hamana T., Hattori M., Ebeling H., Henry J. P., Futamase T., Shioya Y., 1997, ApJ, 484, 574
Holtzman J. A., Burrows C. J., Casterano S., Hester J. J., Trauger J. T., Watson A. M., Worthey G., 1995, PASP, 107, 1065
Kneib J.-P., Mellier Y., Fort B., Mathez G., 1993, A&A, 273, 367
Kneib J.-P., Mathez G., Fort B., Mellier Y., Soucail G., Longaretti P.-Y., 1994, A&A, 286, 701
Kneib J.-P., Ellis R. S., Smail I., Couch W. J., Sharples R. M., 1996, ApJ, 471, 643
Lilly S. J., Tresse L., Hammer F., Crampton D., Le Fevre O., 1995, ApJ, 455, 108
Lowenthal J. D. et al., 1997, ApJ, 481, L673
Lucy L., 1974, AJ, 79, 745
Mellier Y., Soucail G., Fort B., Le-Borgne J.-F., Pello R., 1990, in Mellier Y., Fort B., Soucail G., eds, Gravitational Lensing. Springer, Berlin, p. 261
Mellier Y., Fort B., Kneib J.-P., 1993, ApJ, 407, 33
Press W. H., Teukolsky S. A., Vettering W. T., Flannery B. P., 1992, Numerical Recipes. Cambridge Univ. Press, Cambridge
Schneider P., 1996, A&A, 283, 837
Schneider P., Seitz C., 1995, A&A, 294, 411
Schneider P., Ehlers J., Falco E., 1992, Gravitational Lenses. Springer, Heidelberg
Seitz C., Kneib J. P., Schneider P., Seitz S., 1996, A&A, 314, 707
Smail I., Hogg D. W., Yan L., Cohen J. G., 1995, ApJ, 449, L105
Steidel C. C., Giavalisco M., Pettini M., Dickinson M., Adelberger K. L., 1996a, ApJ, 462, 17
Steidel C. C., Giavalisco M. M., Dickinson M., Adelberger K. L., 1996b, AJ, 112, 352
Trager S. C., Faber S. M., Dressler A., Oemler A., Jr, 1997, ApJ, 485, 92
Williams L. L. R., Lewis G. F., 1997, MNRAS, 281, L35 (WL)
Yee H. K. C., Ellingson E., Bechtold J., Carlberg R. G., Cuillandre J.-C., 1996, AJ, 111, 1883 (Y96)
Ziegler B., 1996, PhD thesis, Univ. Heidelberg
Ziegler B., Bender R., 1997, MNRAS, in press (astro-ph/9704280)

APPENDIX A: THE DEFLECTION POTENTIAL OF THE CLUSTER AND THE GALAXIES

We model the deflection potential of the cluster, the cD galaxy and other individual galaxies by an elliptical non-singular isothermal deflection potential with a velocity dispersion σ, a core radius ζ, a major axis orientation angle ϕ and an ellipticity parameter ϵ (in units of km s^{-1} arcsec and degrees with respect to the x-axis):

$$\psi(\tilde{x}, \tilde{y}) = \psi_0 \sqrt{1 + q_\psi \left(\frac{\tilde{x}}{\zeta}\right)^2 + \frac{1}{q_\psi}\left(\frac{\tilde{y}}{\zeta}\right)^2}. \tag{A1}$$

Here, $\tilde{x}$ and $\tilde{y}$ denote pixel positions with respect to the centre of mass, the $\tilde{x}$-axis is parallel to the major axis of the potential and $q_\psi = (1-\epsilon)/(1+\epsilon)$ is the axis ratio of equipotential contours. The normalization $\psi_0 = \theta_E \zeta$ depends on the Einstein radius

$$\theta_E = 4\pi \left(\frac{\sigma}{c}\right)^2 \frac{D_{ds}}{D_s}, \tag{A2}$$

where c is the speed of light while the source redshift and the cosmological parameters enter in the angular diameter distances from the cluster to the source (D_{ds}) and the observer to the source (D_s). At redshift z the Einstein angle becomes

$$\theta_E \approx \left(\frac{\sigma}{49 \text{ km s}^{-1}}\right)^2 \frac{D_{ds}(z)}{D_s(z)}\left[\frac{D_{ds}(\text{cB58})}{D_s(\text{cB58})}\right]^{-1} \text{ pixel}$$

$$\approx \left(\frac{\sigma}{220 \text{ km s}^{-1}}\right)^2 \frac{D_{ds}(z)}{D_s(z)}\left[\frac{D_{ds}(\text{cB58})}{D_s(\text{cB58})}\right]^{-1} \text{ arcsec} \tag{A3}$$

for an Einstein–de Sitter universe and increase by a factor of ≈ 1.4 for a flat universe with $\Omega = 0.3$. Any quoted value of velocity dispersion assumes an Einstein–de Sitter cosmology.

The deflection angle α, surface mass density κ, shear $\gamma = \gamma_1 + i\gamma_2$ and magnification μ of a point source can be obtained as first- and second-order derivatives of the deflection potential with respect to the angular coordinates $\tilde{x}$ and $\tilde{y}$ (Schneider et al. 1992):

$$\alpha_i = \psi_{,i}, \qquad \kappa = \frac{1}{2}(\psi_{,22} + \psi_{,11}), \tag{A4}$$

$$\gamma_1 = \frac{1}{2}(\psi_{,22} - \psi_{,11}), \qquad \gamma_2 = -\psi_{,22}, \tag{A5}$$

$$\mu^{-1} = (1-\kappa)^2 - |\gamma|^2. \tag{A6}$$

With $C = \psi/\psi_0$, $Q = (q_\psi + 1/q_\psi)$ and $\bar{Q} = (1/q_\psi - q_\psi)$ these functions become

$$\kappa = \frac{1}{2C^3}\left\{Q + \frac{\tilde{x}^2 + \tilde{y}^2}{\zeta^2}\right\}\frac{\theta_E}{\zeta}, \tag{A7}$$

$$\gamma_1 = \frac{1}{2C^3}\left\{\bar{Q} + \frac{\tilde{X}^2 - \tilde{Y}^2}{\zeta^2}\right\}\frac{\theta_E}{\zeta}, \tag{A8}$$

$$\gamma_2 = \frac{1}{2C^3} \left\{ \frac{2\tilde{x}\tilde{y}}{\zeta} \right\} \frac{\theta_E}{\zeta}. \tag{A9}$$

The mass distribution has the following properties.

(i) It simplifies to the mass profile of a singular isothermal sphere, $\kappa \approx \theta_E/(2\sqrt{\tilde{x}^2 + \tilde{y}^2})$, if the mass distribution is spherically symmetric $(q_\psi = 1)$ and if positions with $\tilde{x}^2 + \tilde{y}^2 \gg \zeta^2$ are considered.

(ii) For an isopotential axis ratio q_ψ the mass within an *ellipse* of the same axis ratio q_ψ and area πr^2 equals

$$M_r(q_\psi) = \pi \theta_E \zeta \left\{ \frac{Q - 1 + Q/2 \ (r/\zeta)^2}{\sqrt{1 + (r/\zeta)^2}} + 1 - Q \right\}. \tag{A10}$$

Hence, for an elliptical potential the ratio of the mass within an ellipse of axis ratio q_ψ and area πr^2 to the mass $M_r^0 = M_r(q_\psi = 1)$ within a circle of radius r and a circular potential is given by

$$\frac{M_r(q_\psi)}{M_r^0} = \frac{Q - 1 + Q/2 \ (r/\zeta)^2 + \sqrt{1 + (r/\zeta)^2} \ [1 - Q]}{1 + (r/\zeta)^2 - \sqrt{1 + (r/\zeta)^2}}; \tag{A11}$$

this ratio equals 1 at $r = 0$, increases monotonically with increasing r and becomes

$$\lim_{(\xi) \to \infty} \frac{M_r(q_\psi)}{M_r^0} = \frac{1}{2} Q = \left[q_\psi + \frac{1}{q_\psi} \right] \frac{1}{2} \gtrsim 1 \tag{A12}$$

for $r^2 \gg \zeta^2$. Thus models with the same velocity dispersion σ but different ϵ have different isodensity *shapes* but the same 'mean' mass density (measured within ellipses with an axis ratio given by the potential). We want to point out that the 'velocity dispersion' σ derived from the amplitude $\psi_0 = \theta_E \zeta$ has a straightforward relation to the observed velocity dispersion of cluster galaxies only in the spherically symmetric case. Nevertheless we express the estimated amplitude in terms of the velocity dispersion of the cluster.

(iii) For small eccentricities of the cluster potential $\epsilon_{cl} < 0.2$, the isodensity contours are roughly elliptical and the axis ratio

$$q_\kappa = \frac{1 - \hat{\epsilon}_{cl}}{1 + \hat{\epsilon}_{cl}} \tag{A13}$$

of the isodensity contours is related to the isopotential contours according to $\hat{\epsilon}_{cl} \approx 3\epsilon_{cl}$.